Climatology of the San Francisco Bay and the Initiation of Wind Reversals along the Western United States Coast Determined from AMDAR Data

By

Dillon Turner
B.Sc., Arizona State University, 2015

Submitted to the graduate degree program in Geography and Atmospheric Science and the Graduate Faculty of the University of Kansas in partial fulfillment of the requirements for the degree of Master of Science.

_____

Chair: David Rahn

_____

David Mechem

_____

Nathaniel Brunsell

Date Defended: 2 May 2018

The thesis committee for Dillon Turner certifies that this is the approved version of the following thesis:

Climatology of the San Francisco Bay and the Initiation of Wind Reversals along the Western United States Coast Determined from AMDAR Data

_____

Chairperson: David Rahn

Date Approved: 4 May 2018

ABSTRACT

Observations from commercial aircraft through the Aircraft Meteorological Data Relay (AMDAR) automated weather reports provide a higher frequency sampling of the lower atmosphere than the twice daily radiosonde launches performed by the National Weather Service. In the San Francisco Bay area, the number of profiles from flights arriving or departing San Francisco International Airport (SFO), Oakland International Airport (OAK), and San Jose International Airport (SJC) have increased dramatically from 2001 to 2016. Low-level features in the coastal margins are difficult to simulate, so AMDAR opens up new possibilities to investigate coastal phenomena. This study uses AMDAR measurements from 2001-2016 in the bay area and focuses on three main objectives: (1) understanding the AMDAR climatology of the lower atmosphere in the bay area, (2) examining the effectiveness of AMDAR data to identify and quantify precursors to wind reversals along the central California coast, and (3) use the quantified magnitudes of the precursors to forecast wind reversals. A limiting factor in past studies of wind reversals was the lack of long-term monitoring of the lower atmosphere. While soundings from the aircraft at OAK and SFO were similar and more influenced by the marine environment, SJC had more continental features. Significant anomalies of temperature and wind occurred more than 24 hours ahead of the passage of a wind reversal. A forecast metric was developed using the anomalies, but the metric was not skillful.

ACKNOWLEDGMENTS

First, I would like to thank my advisor Dr. David Rahn for everything that he has done for me throughout this journey. I am truly appreciative of him for allowing me to have this opportunity and work with him on this project. I would also like to thank the rest of my committee, Dr. Nathaniel Brunsell and Dr. David Mechem for all their support and guidance along the way. Besides my committee, I would like to thank my family for believing in me and pushing me to achieve my dreams. Lastly, I want to thank all my friends in Pennsylvania, Arizona, and Kansas for being there for me through the stressful and not so stressful times over the past 3 years.

TABLE OF CONTENTS

Page

ABSTRACT iii

ACKNOWLEDMENTS iv

TABLE OF CONTENTS v

LIST OF FIGURES vii

LIST OF TABLES x

Chapter 1: Introduction 1

1.1 Introduction 1

1.2 Motivation and Objectives 4

Chapter 2: Data and Methods 8

2.1 AMDAR 8

2.2 NWS Radiosonde Soundings 10

2.3 Buoy 10

2.4 Satellite 12

2.5 Reanalysis 12

Chapter 3: Climatology of the San Francisco Bay 13

3.1 Mean Synoptic Conditions from NARR 13

3.2 Mean Profiles from AMDAR 14

a. BL Heights 18

i) OAK 18

ii) SFO 21

iii) SJC 21

b. Diurnal Cycle of Temperature and Wind 22

3.3 Representativeness of AMDAR 28

Chapter 4: Wind Reversals 33

4.1 Anomalies 33

4.2 Significance 34

4.3 Anomaly Forecast Metric 36

4.4 Trend Forecast Metric 39

Chapter 5: Summary and Conclusions 43

REFERENCES 46

APPENDIX 48

LIST OF FIGURES

1.1: NARR mean upper air composite maps at 500 hPa, 850 hPa, and 1000 hPa leading up to the start of wind reversals 3

1.2: Map of central California and the San Francisco Bay with buoy and airport locations 7

2.1: Total number of soundings each year at each airport. 9

3.1: NARR upper air composite maps of the climatological conditions of the western United States and the eastern Pacific in June from 2001-2016. (a) 300 hPa (b) 500 hPa (c) 700 hPa (d) 850 hPa (e) 925 hPa 14

3.2: Density plot of the log of the AMDAR point observations (2001-2016) where the BL was detected in 0.01° x 0.01 bins from flights arriving or departing OAK, SFO, and SJC 15

3.3: For 2001-16, the average number of total soundings (blue bar) and soundings with a detected boundary layer (red bar) each hour per day in June for (a) SFO, (b) OAK, and (c) SJC. The solid blue line is the fraction of soundings with a detected boundary layer. The vertical dashed bars indicate the sunrise and sunset on 15 June..... 17

3.4: Boxplots of boundary layer depth (m) at (a) OAK, (b) SFO, and (c) SJC for June 2001-2016. The median is the red horizontal line, the mean is the x, the box contains the interquartile range, and the whiskers extend to the 10th and 90th percentiles. The numbers at the top indicate the total number of soundings included in each hourly bin. The vertical dashed bars indicate the sunrise and sunset on 15 June..... 19

3.5: The diurnal cycle of the average boundary layer height for all months during the warm season (April-September) at (a) OAK, (b) SFO, and (c) SJC. The vertical dashed bars indicate the sunrise and sunset on 15 June 20

3.6: Time-height cross sections of the temperatures at (a) OAK, (b) SFO, and (c) SJC in June from 2001-2016. The solid black line is the mean BL height for each airport in June. The vertical dashed bars indicate the sunrise and sunset on 15 June..... 23

3.7: Time-height cross sections of the u-winds at (a) OAK, (b) SFO, and (c) SJC in June from 2001-2016. The solid black line is the mean BL height for each airport in June. The vertical dashed bars indicate the sunrise and sunset on 15 June..... 25

3.8: Time-height cross sections of the v-winds at (a) OAK, (b) SFO, and (c) SJC in June from 2001-2016. The solid black line is the mean BL height for each airport in June. The vertical dashed bars indicate the sunrise and sunset on 15 June..... 26

3.9: (a-c) Time-height cross sections of the difference in the (a) temperatures, (b) u-winds, and (c) v-winds at OAK from those at SFO in June. (d-f) Time-height cross sections of the difference in the (d) temperatures, (e) u-winds, and (f) v-winds at OAK from those at SJC in June. The vertical dashed bars indicate the sunrise and sunset on 15 June 27

3.10: Correlation profiles of temperature, u-wind, and v-wind during the warm season between AMDAR observations from OAK and NWS soundings from OAK at (a) 0000 UTC and (b) 1200 UTC..... 28

3.11: Correlation profiles of temperature, u-wind, and v-wind at all hours during the warm season between (a) AMDAR observations at OAK and SFO and (b) AMDAR observations at OAK and SJC 30

3.12: Density plots of OAK's and SFO's temperatures, u-winds, and v-winds during the warm season from 2001-2016 (Top Row) within the BL at 300 m and (Bottom Row) above the BL at 1000 m. Temperatures are binned every 1° C and winds are binned every 1 m s-1. The one to one reference line is shown in black..... 31

3.13: Density plots of OAK's and SJC's temperatures, u-winds, and v-winds during the warm season from 2001-2016 (Top Row) within the BL at 300 m and (Bottom Row) above the BL at 1000 m. Temperatures are binned every 1° C and winds are binned every 1 m s-1. The one to one reference line is shown in black 31

4.1: Time-height cross sections of the mean anomalies of the (a) temperatures, (b) u-winds, and (c) v-winds before, during, and after the start of low threshold wind reversal events from AMDAR observations at OAK and SFO 34

4.2: As in Fig. 4.1 but for high threshold wind reversal events 34

4.3: The solid red line shows the mean anomaly profiles of the (a-d) temperature, (e-h) u-wind, and (i-l) v-wind for 0, 12, 24, and 36 hours before the start of low threshold wind reversal events. Where the solid red lines become thicker is where the mean anomalies of low threshold events are significant at the 0.01 level. The dashed red lines indicate the standard deviations of the mean anomalies. The solid blue line is the zero anomaly line and the dashed blue lines indicate the standard deviations of all observations during the warm season 35

4.4: The solid red line shows the mean anomaly profiles of the (a-d) temperature, (e-h) u-wind, and (i-l) v-wind for 0, 12, 24, and 36 hours before the start of high threshold wind reversal events. Where the solid red lines become thicker is where the mean anomalies of high threshold events are significant at the 0.01 level. The dashed red lines indicate the standard deviations of the mean anomalies. The solid blue line is the zero anomaly line and the dashed blue lines indicate the standard deviations of all observations during the warm season 36

4.5: The solid black line is the mean anomalies of the (a) temperature, (b) u-wind, and (c) v-wind leading up to the start of low threshold wind reversal events. The dashed lines are the 25% and 75% quantiles. The dotted lines are the 10% and 90% quantiles.....39

4.6: As in Fig. 4.5 but for high threshold wind reversal events 39

4.7: The 3, 6, 9, and 12 hourly mean trend of the anomalies of the (a) temperature, (b) u-wind, and (c) v-wind leading up to the start of low threshold wind reversal events.....41

4.8: As in Fig. 4.7 but for high threshold wind reversal events 41

LIST OF TABLES

4.1: Contingency table showing the performance of the anomaly forecast metric..... 37

4.2: Contingency table showing the performance of the trend forecast metric 42

Chapter One

Introduction

1.1) Introduction

During the warm season, the average conditions along the eastern boundary of the North Pacific are characterized by northerly low-level flow that is driven by a pressure gradient associated with the Northeast Pacific High and thermal trough in the desert Southwest (Halliwell et al. 1987). The surface anticyclone typically extends up to 850 hPa with the greatest onshore flow in the Pacific Northwest, and a 500-hPa trough is located just off the west coast (Bond and Mass 1996). Near the surface, the marine boundary layer (MBL) is characterized by cool, moist air underneath a marked temperature inversion created by subsidence aloft that separates the MBL from the warm, dry free troposphere aloft. The MBL can vary substantially, but the average height is 400 m along the California coast and it slopes upward from the coast eventually reaching an average height of 2000 m near the Hawaiian Islands (Neiburger 1960). A coastal low-level jet is often present near the coast with a distinct maximum of wind speed at the top of the MBL.

The normal northerly wind along the coast is periodically interrupted by a southerly wind. These events have been referred to as wind reversals, southerly surges, coastally trapped disturbances, and coastally trapped wind reversals. A southerly wind can be associated with an approaching surface cyclone, but wind reversals can occur when the Pacific high extends further northeast of its climatological center and prompts a mesoscale response near the shore. The term wind reversal will refer exclusively to the latter situation. Wind reversals can occur along the coast from southern California to the Canadian border during the warm season (April-

September). On average, they occur about 1-2 times a month and can last from a few hours to a couple days (Bond et al. 1996). The reversal of the surface wind is often accompanied by a surge of fog or a shallow, cloudy marine layer that progresses northward along the coast and disrupts land, sea, and air travel. Initiation and the dynamics of coastal wind reversals are not fully understood and have been widely debated (e.g., Nuss et al. 2000), which contributes to the difficulty in forecasting these events.

Preceding a wind reversal, the synoptic conditions shift from their more climatological state and become favorable for the development of a wind reversal (Fig. 1.1). This evolution occurs on average 48 hours prior to a wind reversal but has been seen to occur as early as a week before an event (Bond and Mass 1996). Prior to the initial wind reversal, the 500-hPa trough moves into the Pacific Northwest with its axis positively tilted offshore of southern California and a ridge builds along the western Canadian coast. The 500-hPa trough becomes cutoff and the ridge drifts slightly eastward. At 850 hPa, the ridge moves inland as well and results in enhanced offshore flow. As the 850-hPa ridge moves inland a strong positively tilted trough develops along the coast becoming cutoff by the start of the event. At the surface, the Northeast Pacific High intensifies and moves inland towards the Pacific Northwest. The thermal trough in California extends northwestward along the coast because of warm air advection and subsiding flow from the continent. The extension of the surface trough northwestward produces an anomalous pressure gradient force directed northward along the coast. Even when conditions are similar to those just described, a wind reversal is not guaranteed.

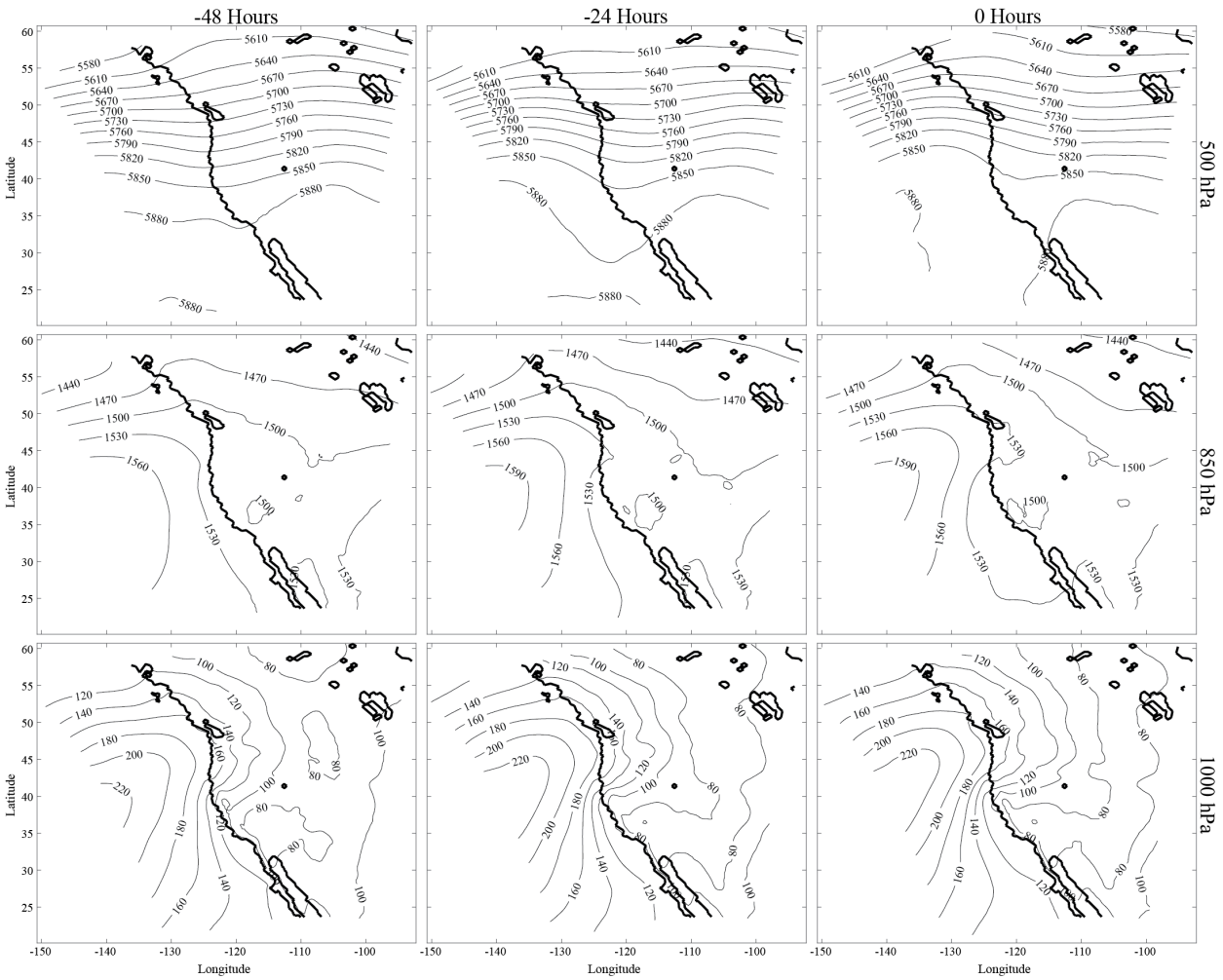

Fig. 1.1 NARR mean upper air composite maps at 500 hPa, 850 hPa, and 1000 hPa leading up to the start of wind reversals

Initiation of a wind reversal occurs as a mesoscale response to the synoptic forcing. The two-layer fluid system consisting of a MBL and free troposphere above is bounded on one side by the coastal topography, which allows for several classes of mesoscale phenomena. Dorman (1987) suggests the initiation mechanism is a simultaneous deepening of the MBL to the south while the MBL lowers to the north and is associated with a weak cyclonic circulation. Bond and Mass (1996) suggest that it is just the rapid reduction in thickness of the marine layer to the north

that initiates the wind reversal. Both of the proposed initiation mechanisms are fundamentally the result of mid-level offshore winds creating a northward decreasing pressure gradient (Skamarock et al. 1999). The reversal of the normal pressure gradient causes a northward acceleration, initiating the wind reversal and northward surge of a deeper MBL. The northward propagation of the deeper MBL has been proposed to act as a Kelvin wave (Dorman 1985) or a gravity current (Bond and Mass 1996). Both mechanisms rely on a higher MBL height to the south that is associated with a northward pressure gradient force and topographic blocking of the fluid (Dorman 1985). The following key differences between the Kelvin wave and gravity current interpretations were presented in Nuss (2000). First, the linear Kelvin wave interpretation represents a continuous change of marine layer depth across the head of the wind reversal, while the gravity current represents a distinct discontinuity in the marine layer depth. Also, the gravity current's leading edge is characterized by an increase of turbulence, while turbulent motion is not a necessary feature at the Kelvin wave's leading edge. The gravity current's leading edge is associated with a clear equivalent potential temperature difference, while Kelvin waves do not require any temperature difference. Finally, perturbations of the MBL depth that are associated with a Kelvin wave must exponentially decay offshore.

The proposed explanation of the northward progression of a deeper marine layer acting as a Kelvin wave has been disputed by various studies as not accurately defining the characteristics of the propagation. For a Kelvin wave to occur along the coast, there must be a localized offshore wind to create pressure anomalies (Skamarock 1999). Initiation of wind reversals has been shown to be dominated by synoptic forcing rather than mesoscale forcing (Bond and Mass 1996). The mesoscale response to synoptic forcing is illustrated in Bond and Mass (1996) and shows that the composite pressure anomalies that altered the climatological pressure gradients

were not confined to the coastal areas of the trapped marine layer (Bond and Mass 1996). Applying the hydrostatic equation to a large upward displacement of the marine layer by 400 m increases the surface pressure by 1.2 hPa, which is small compared to the climatological pressure gradient of 5 hPa between San Diego and northern California (Bond and Mass 1996). Ralph and Neiman (1998) analyzed the predicted and observed phase speeds of a wind reversal event to understand what explanation best represents these disturbances. The observed phase speed was 13.2 ± 0.6 m s^{-1} while the predicted Kelvin wave speed was 9.3 ± 0.8 m s^{-1} and the predicted propagation speed of the gravity current was 12.6 ± 1.4 m s^{-1} (Ralph and Neiman 1998). The predicted gravity current speed falls within the uncertainty and best represents the actual propagation of the event (Ralph and Neiman 1998). Nuss (2000) supports the gravity current interpretation as well, due to the decrease in surface temperatures at buoys along the Oregon and Washington coasts during wind reversal events. Aircraft observations confirm that the wind reversal has characteristics of a gravity current (Rahn and Parish 2008). The work presented here will use the gravity current interpretation as the underlying forcing mechanism that drives these wind reversals, however, either interpretation does not affect the results as both interpretations are the result of offshore flow to the north causing a lowering of the MBL to the north.

1.2) Motivation and Objectives

Understanding the nearshore environment preceding and during wind reversal events is vital to our understanding of the initiation mechanisms and dynamics of such events. Past research and reanalysis of the climatological conditions of wind reversals have used reanalysis grids that by today's standards are coarse in resolution, such as the 380-km grid spacing used in Bond and Mass (1996). Previous work has also shown discrepancies in the initiation mechanisms and propagation characteristics (e.g., Dorman 1985; Bond and Mass 1996; Skamarock 1999;

Nuss et al. 2000; Nuss 2007). Despite the disagreement on forcing mechanisms, most agree that a change in the MBL depth tied to the offshore wind causes propagation of the wind reversal to the north. Furthermore, current models have difficulty in correctly simulating the MBL near the coast (Angevine et al. 2012) and even well-offshore (Wyant et al. 2010), which can lead to additional uncertainty in any analysis of coastal wind reversal initiation.

Measurements can help clarify the near-coast environment associated with wind reversals. Aircraft Meteorological Data Relay (AMDAR) automated weather reports from the Aircraft Communications Addressing and Reporting System (ACARS) were analyzed for past wind reversal events during the warm season from 2001 through 2016. With this data, soundings were obtained from all flights departing or arriving at San Francisco International Airport (SFO), Oakland International Airport (OAK), and San Jose International Airport (SJC) before, during, and after a wind reversal event (Fig. 1.2). The soundings allow the boundary layer (BL) depth to be identified and changes to the lower atmosphere over time to be detected at a higher temporal resolution then the daily 0000 and 1200 UTC National Weather Service (NWS) soundings. Changes in the low-to mid-level flow were analyzed to determine the strength and persistence of offshore flow preceding wind reversals. Geostationary Operational Environmental Satellite (GOES) imagery was used to determine whether the southerlies were a result of a wind reversal event or associated with a synoptic scale system such as a migrating cyclone.

There are three main objectives of this work. The first objective is to use AMDAR to create a climatological profile of the San Francisco Bay during the warm season. The second objective is to use the AMDAR climatology to quantify the magnitude of offshore flow and temperature anomalies above the BL during coastal wind reversals in central California. The third objective is to use the quantified magnitudes of the anomalies to forecast wind reversals.

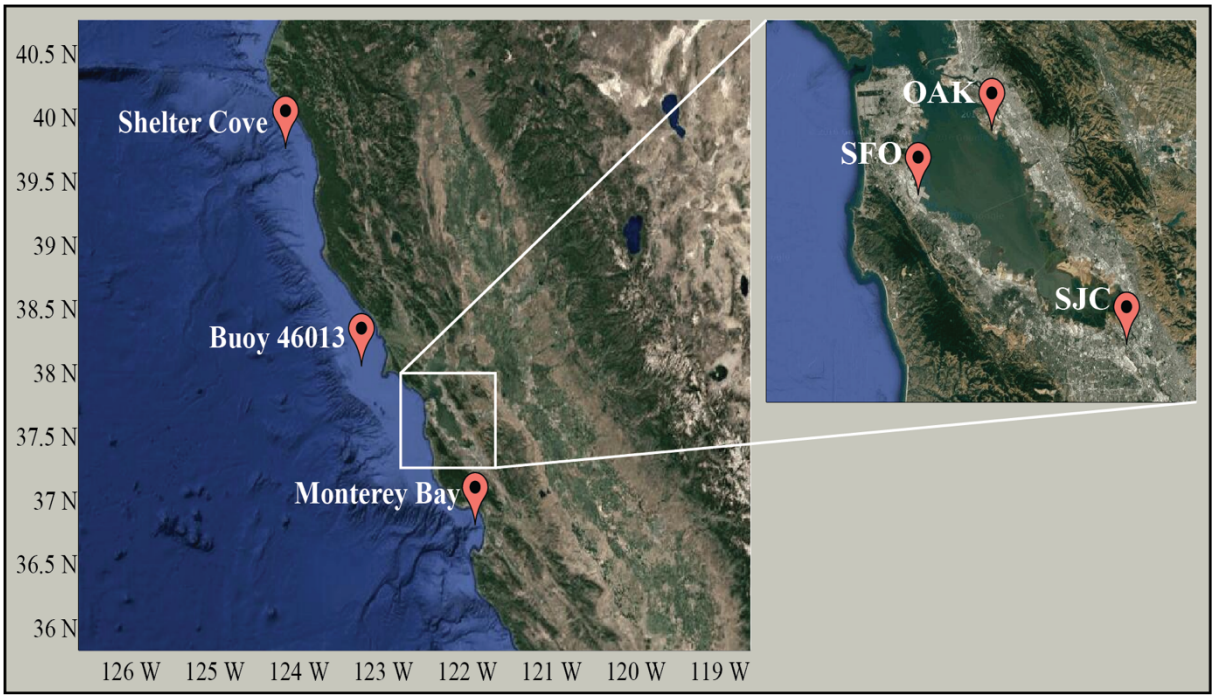

Fig. 1.2: Map of central California and the San Francisco Bay with buoy and airport locations.

Chapter Two

Data and Methods

2.1) AMDAR

Archived AMDAR observations are available through the Meteorological Assimilation Data Ingest System (MADIS). The point measurements are archived every hour, creating 24 files each day. Data is provided in two formats. One format has all raw data and the other format has only data collected during ascent and descents, which removes data during level flight. The files with all of the raw data are used to create soundings and follow the methods in Rahn and Mitchell (2016). Since only low-level observations in central California are relevant, subsets of the data were made to extract only observations below 3 km near SFO, OAK, and SJC. Aircraft tail numbers were used to link the point observations to individual flights and grouped into consecutive measurements with no time gaps larger than 2 minutes. In order for a sounding to qualify, there must have been at least ten observations and at least one observation within 200 m of the surface. To link flights to their specific airport, polygons were made around each airport based on their latitude and longitude. The lowest observations from each flight were used to assign it to an airport based on which polygon it was located in.

The total number of soundings created from 2001 through 2016 for SFO, OAK, and SJC combined was 511,871. OAK is responsible for most of the soundings between 2001 and 2009, but SFO and SJC contribute a substantial amount from 2010 to 2016 (Fig. 2.1). The number of soundings has drastically increased since 2001 due in part to more airlines adopting the system. In 2001, the number of soundings per day at each airport ranged from 0-6 and in 2016 the number of soundings per day was as many as 152 at OAK. As more airlines adopt the AMDAR

system more soundings and a greater frequency of the atmospheric profile throughout the day can be made.

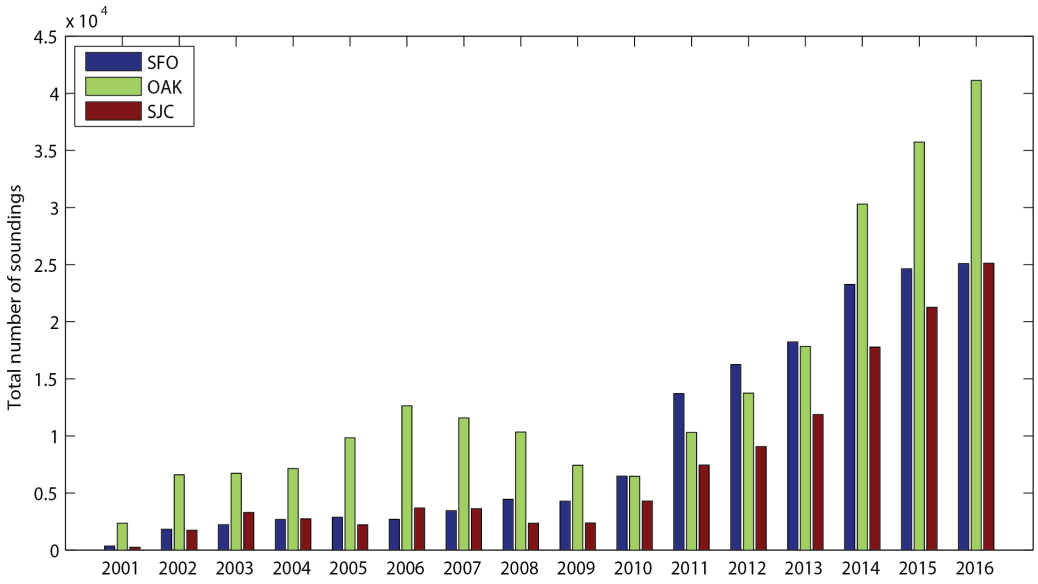

Fig. 2.1: Total number of soundings each year at each airport.

Vertical position of the aircraft is recorded as the pressure altitude. However, since surface pressure changes on diurnal, synoptic, and seasonal scales, height above the ground was chosen as the preferred vertical position. To get height above the ground, the static pressure measurement was retrieved using the pressure altitude and standard atmosphere. Then, the surface pressure and temperature were obtained from the surface meteorological station at the corresponding airport. Due to the necessity of accurate measurements around the airport the surface meteorological stations have a high degree of accuracy and reliability. The height above the ground was found by using the hypsometric equation and the airport station pressure, temperature, and elevation. Finally, the heights were interpolated to a regular grid from the surface to 3000 m at an interval of 20 m.

To find the height of the BL, the lapse rate of temperature was calculated for all observations above 100 m from the surface. Observations below 100 m were ignored due to the common occurrence of a surface radiation inversion in the morning. The BL height was defined as the height of the minimum temperature below the strongest inversion. No BL height is reported if there is no temperature inversion, if the inversion is too weak (<1 K km^{-1}), or if the inversion extends to the surface.

Mean hourly soundings for each month were created from the AMDAR observations to account for the diurnal cycle and its variability throughout the warm season. To remove the diurnal and seasonal cycles the wind and temperature anomalies were computed. Sounding temperatures, v-winds, and u-winds 72 h before to 72 h after a wind reversal were subtracted from the mean sounding for the corresponding hour and month. Anomalies of the temperature and wind profiles were then composited relative to the initial time of the wind reversal.

2.2) NWS Radiosonde Soundings

Radiosonde data launched from OAK by the NWS were obtained from NOAA and the Earth System Research Laboratory (ESRL). Observations were obtained from both the 0000 UTC and 1200 UTC launches throughout the study period. Similar to the AMDAR observations, the radiosonde observations were linearly interpolated from the surface up to 3000 m at regular intervals of 20 m. The height of the BL was defined with the same method as the AMDAR data.

2.3) Buoy

Surface observations are obtained from the National Data Buoy Center (NDBC). Buoy 46013 was used for this analysis and is located off the coast to the northwest of the San Francisco Bay and Point Reyes, CA (Fig. 1.2). Buoy 46013 is of most importance due to its

proximity to San Francisco and its well-maintained historical observations. Observations of wind speed and direction were used to determine the onset of a wind reversal. The wind speed and direction were used to find the alongshore and cross shore wind components to facilitate the physical interpretation. The coastal orientation near Buoy 46013 is 133° (Halliwell et. al 1987), measured in degrees counterclockwise from due east.

To create the most robust list of wind reversal events, two classification schemes were considered. Both schemes determine whether a reversal occurred based on the magnitude of the southerly flow at buoy 46013. The first scheme classified events as either strong or weak events. This classification followed the Bond and Mass (1996) criteria. For strong events: (1) prior to the time of the wind reversal there were at least 12 hours of northerly flow, (2) the onset time of the reversal was the first hour with a southerly component for which southerly flow was observed for at least 9 out of the next 11 hours, (3) during at least 1 hour the southerly component attained a speed of at least 5 m s^{-1}, (4) and the average wind direction had to be within 45° of the orientation of the coastline during the first 11 hours after the wind shift. For weak events the southerly component was required to stay below 5 m s^{-1}. This criterion appeared to be too stringent and did not effectively discriminate between both events. Also, weak reversal events could not be accurately analyzed because too many weak events were detected that were not able to be confirmed to be classic wind reversals through satellite imagery. These falsely detected weak events are the result of the criterion for weak reversals being set too low leading to ambiguous events. Therefore, only strong events were reviewed. Due to the issues with Bond and Mass's (1996) classification scheme, a new classification scheme was created by lowering the threshold of southerly flow to 3 m s^{-1} and only classifying observations as either wind reversal events or non-events. 3 m s^{-1} was chosen as a better cutoff for wind reversal events after

manually analyzing weak reversal events. For the remainder of this paper, events using Bond and Mass's (1996) classification are referred to as high threshold events and events using the new classification scheme are low threshold events. Lists of the low and high threshold events from 2001-2016 are available in the Appendix.

2.4) Satellite

Archived GOES satellite data is available through the National Oceanic and Atmospheric Administration's (NOAA) Comprehensive Large Array-Data Stewardship System (CLASS). GOES satellite visible and infrared imagery were obtained for times before, during, and after wind reversal events and manually analyzed to distinguish between synoptic (mainly surface cyclones) and coastal wind reversal events. Events that appeared to be influenced by a synoptic scale system (e.g., a land-falling cyclone) were discarded.

2.5) Reanalysis

The North American Regional Reanalysis (NARR) was obtained from NOAA's National Center for Atmospheric Prediction (NCEP) and used to construct composite maps of the climatological conditions over the western United States and eastern Pacific. NARR was used because of its high spatial and temporal resolution (32-km grid spacing, every 3 hours). Wind, temperature, and geopotential heights are available for every 25 hPa below 750 hPa and every 50 hPa above 750 hPa.

Chapter Three

Climatology of the San Francisco Bay

3.1) Mean Synoptic Conditions from NARR

Since June is a fairly representative month of the warm season, the following climatology will focus only on June for brevity. During June, the 300-hPa flow is fairly zonal across the coast of central California (Fig. 3.1a). At 500 hPa, the trough is located just off the coast of California with a ridge near the eastern side of the Rockies (Fig. 3.1b). The desert southwest can be identified at 700 hPa by temperatures >12°C in this region (Fig. 3.1c). A trough is also identifiable at 700 hPa along the coast. The surface thermal low in the desert southwest can be seen at 850 hPa (Fig. 3.1d). Along the coast of California, flow is northerly as a result of the high pressure to the west and trough along the coast. At 925 hPa, the northerly flow is strongest just off the coast of central California (Fig. 3.1e). The thermal low is also identified by the 740 m geopotential heights in the central California valley.

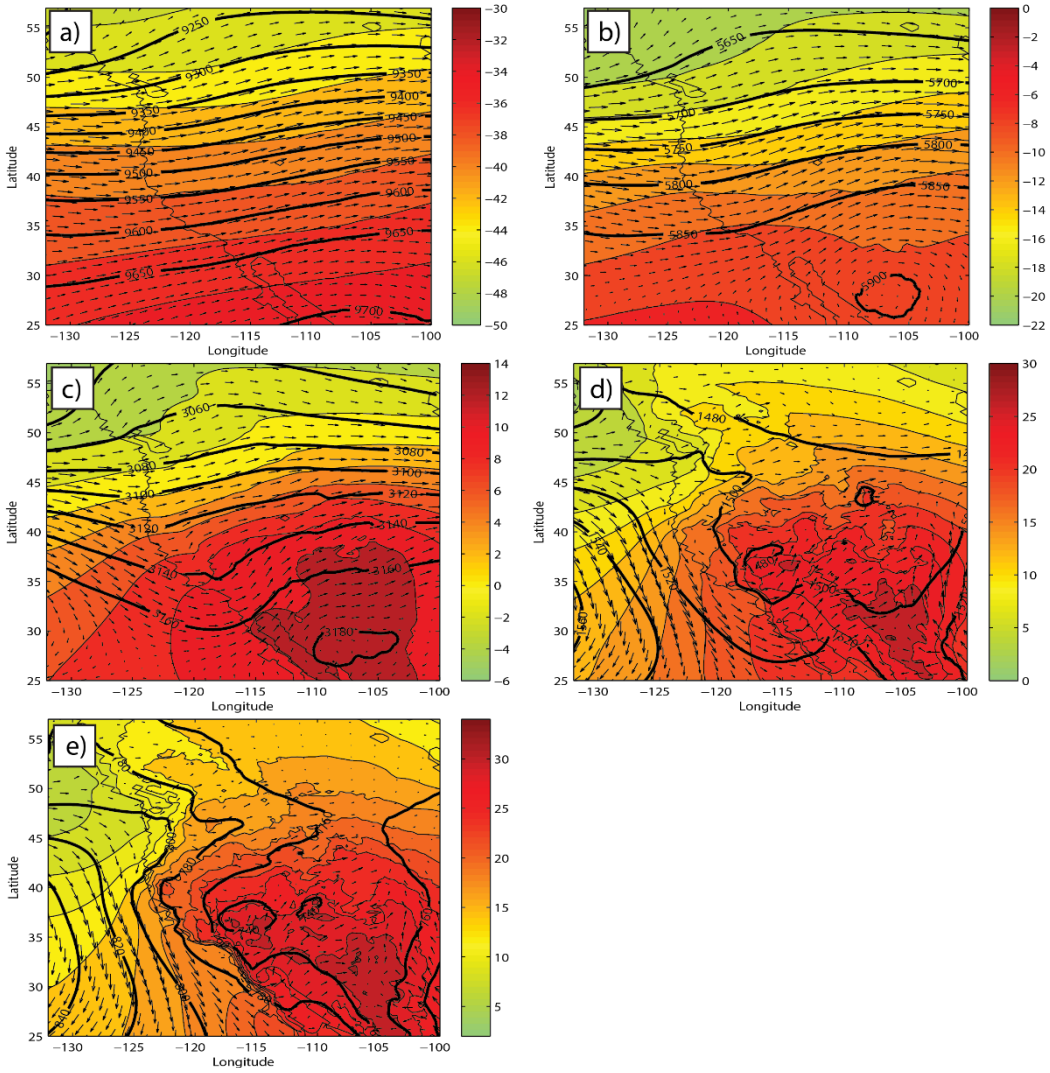

Fig. 3.1: NARR upper air composite maps of the climatological conditions of the western United States and the eastern Pacific in June from 2001-2016. (a) 300 hPa (b) 500 hPa (c) 700 hPa (d) 850 hPa (e) 925 hPa

3.2). Mean Profiles from AMDAR

Observations of the lower atmosphere are an important source of information considering the model uncertainty in the coastal margin (Angevine et al. 2012). AMDAR provides a higher temporal resolution than the twice daily radiosonde launches at OAK and there is a substantial amount of data available to complete a detailed climatological analysis of this region. The log of density plot (Fig. 3.2) indicates the location where the BL was detected for each flight from SFO,

OAK, and SJC. A general sense of flight corridors for each airport can be detected due to the close proximity of the detected BLs and their corresponding airport. The majority of the BLs detected from SFO and OAK flights are to the northwest of the corresponding airport, however, there are some observations to the southeast of both airports. The BL observations for OAK and SFO are either over the San Francisco Bay or in close proximity to the bay. BL observations for SJC flights are generally to the southeast of the airport. The tracks for SJC flights rarely go over the bay and usually go southeast through the valley. Even though the profiles are obtained from three airports less than 50 km apart, the profiles may be representative of only their local region instead of the entire bay area. If that is the case, then observations from each airport must be treated separately. Otherwise, all observations can be included in the subsequent analysis. The representativeness of the AMDAR observations to a marine San Francisco Bay environment will be analyzed later in this section.

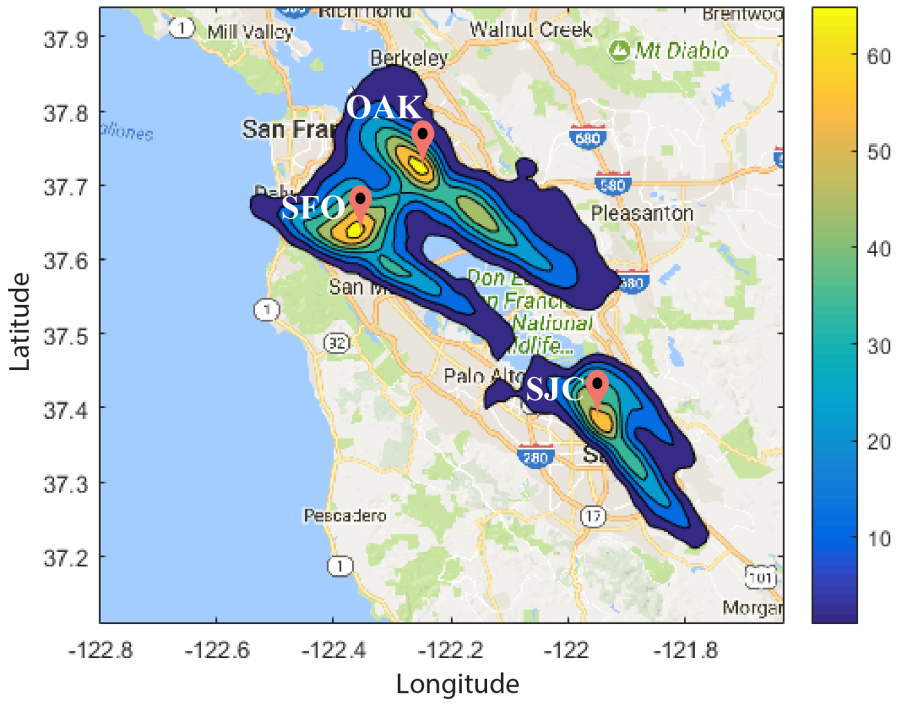

Fig. 3.2: Density plot of the log of the AMDAR point observations (2001-2016) where the BL was detected in 0.01° x 0.01 bins from flights arriving or departing OAK, SFO, and SJC.

The total number of AMDAR observations has drastically increased from 2001 to 2016 (Fig. 2.1). In 2001 the total number of soundings at all three airports combined was less than 5,000. The total number of soundings in 2016 was over 90,000. Observations from planes arriving or departing OAK have been more than SFO and SJC for all years, except 2011-2013 when SFO surpassed OAK observations. Figure 3.3 shows the distribution of sampling from the aircraft at each airport throughout the course of the day in June. Unlike the normal 0000 UTC and 1200 UTC radiosonde launches the AMDAR measurements provide a profile of the atmosphere throughout most of the day. A much smaller number flights land or take off late at night or before dawn. This gap in observations is worse at SJC with fewer flights than OAK and SFO between 0700 UTC and 1200 UTC. OAK has a higher average number of soundings per hour than SFO and SJC with many more between 0900-1200 UTC. At 0600 UTC, OAK experiences the fewest number of soundings detecting an BL with 62% of flights detecting one. SFO experiences their minimum of 60% of flights detecting an BL a few hours later, between 0800-1000 UTC. Detecting an BL during the night and early morning is more difficult when a nocturnal temperature inversion develops at the surface. A lack of observations at SJC during the early morning hours hinders an accurate analysis of the percentage of observations with an BL between 0700-1200 UTC. The number of soundings with a defined BL increases throughout the day to a maximum at 1600 UTC at SFO and 1400 UTC at OAK, where over 80% of the soundings have a defined BL. After 1600 UTC at SFO and 1400 UTC at OAK, the percentage of soundings with a BL continually decrease to their minimum in the early morning hours. SJC has a maximum percentage of soundings with an BL at 0800 UTC, but there are only 3 soundings at this time over the entire period. Dismissing the 0700-1200 UTC observations, the maximum percentage occurs at 1600 UTC with over 90% of flights with a defined BL. Ignoring the gap at

SJC in the early morning, all three airports have a clear diurnal cycle to the percentage of detected BL heights, but an BL is detected ~75% of the time.

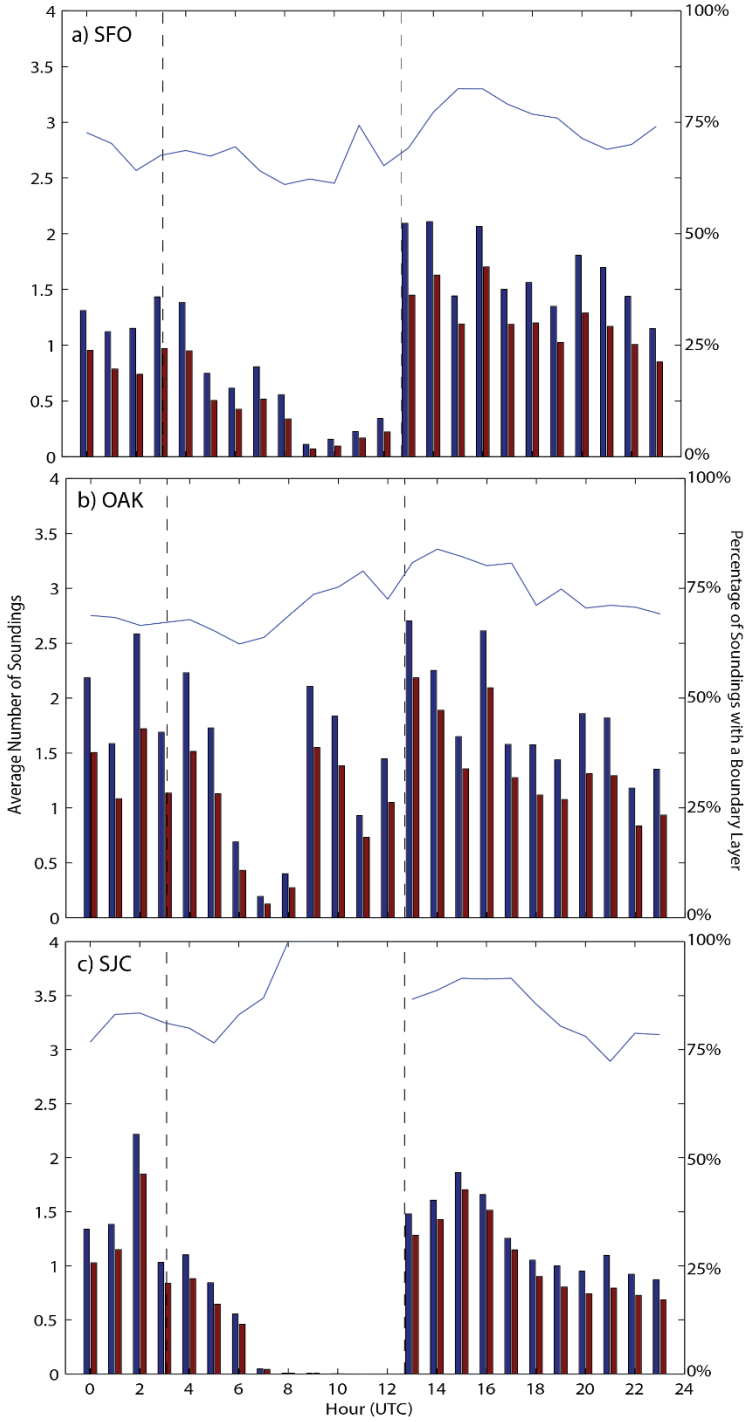

Fig. 3.3: For 2001-16, the average number of total soundings (blue bar) and soundings with a detected boundary layer (red bar) each hour per day in June for (a) SFO, (b) OAK, and (c) SJC. The solid blue line is the fraction of soundings with a detected boundary layer. The vertical dashed bars indicate the sunrise and sunset on 15 June.

a) BL Heights

To analyze the distribution of boundary layer heights at each airport, boxplots were created for the hourly observations in June. The observations were originally separated into cloudy and clear conditions. In June surface observations at SFO reported cloudy conditions only 15.1% of the time while observations at OAK reported cloudy conditions 32.7% of the time. SJC reported cloudy conditions 10.6% of the time in June. Since there are few cloudy days, the total observations were used. This does skew the diurnal cycles to more clear events but since the climatology will be used to look at wind reversals, which are often preceded by clear weather, it does result in a better analysis. The diurnal cycle of the BL heights for all months during the warm season was also plotted to analyze the variation in BL heights throughout the season.

i) OAK

At OAK there are ample soundings at most hours. For example, there are a total of 1,049 soundings available for 1300 UTC in June (Fig. 3.4a), which is an average of 2.2 soundings per day. Off-peak hours such as 0700 UTC have only 60 soundings available from 2001 to 2016. The boxplots indicate that the observations of BL heights are skewed slightly toward higher heights since the mean is higher than the median. The diurnal cycle is also evident with the highest BL heights occurring in the morning hours. After the time of highest BL heights, the BL heights decrease and then become steady between 1500 and 1800 UTC. Following 1800 UTC they decrease again. Lowest BL heights occur around dusk at 2300 UTC. The interquartile range is smallest around dusk as well, indicating less variability in BL heights in the afternoon. All OAK soundings have a mean BL height of 418 m, a median of 375 m, and a standard deviation of 250 m.

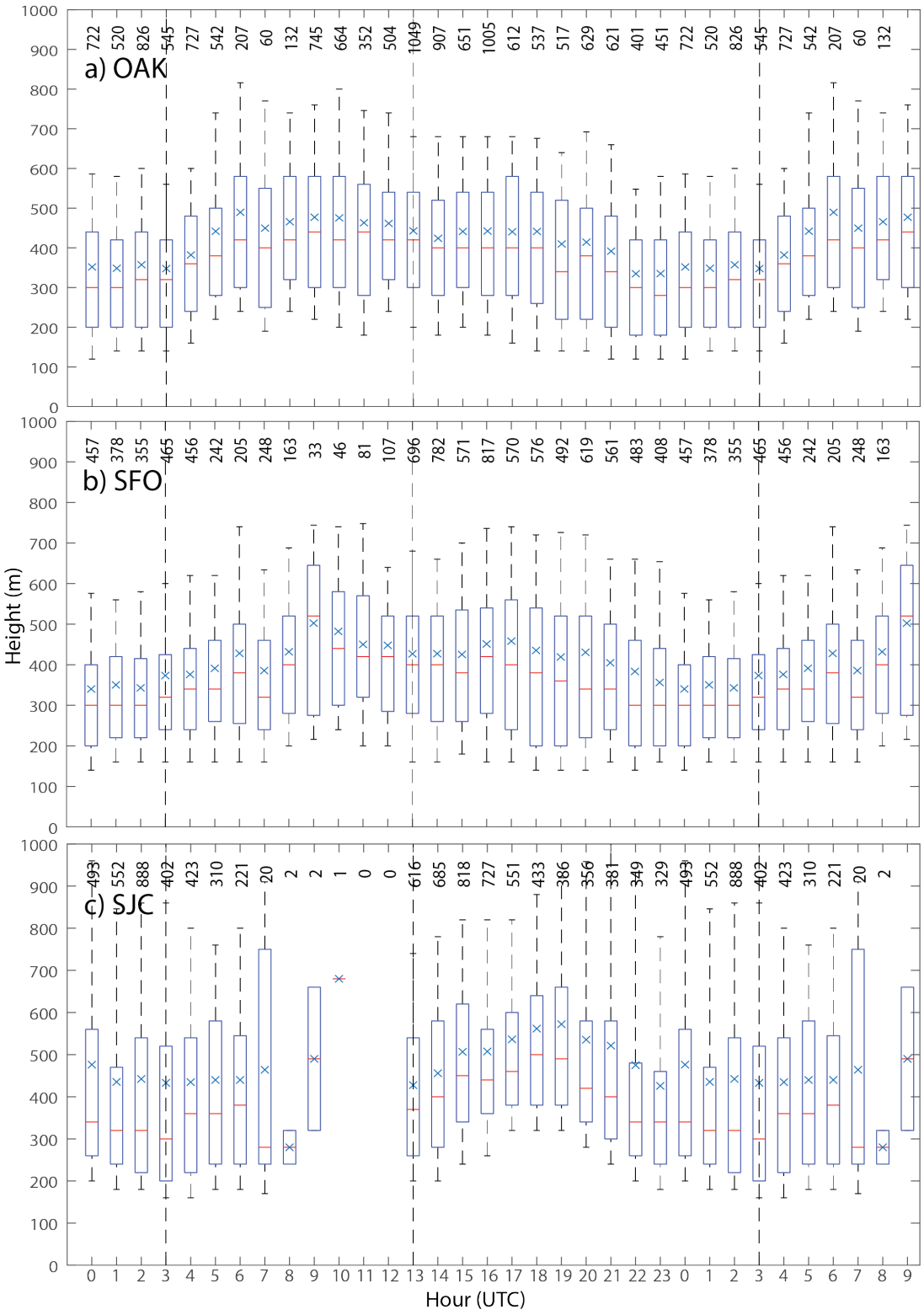

Fig. 3.4: Boxplots of boundary layer depth (m) at (a) OAK, (b) SFO, and (c) SJC for June 2001-2016. The median is the red horizontal line, the mean is the x, the box contains the interquartile range, and the whiskers extend to the 10th and 90th percentiles. The numbers at the top indicate the total number of soundings included in each hourly bin. The vertical dashed bars indicate the sunrise and sunset on 15 June.

Figure 3.5a illustrates the month to month variation in BL heights at OAK. During the warmest months (June-September) the BL heights and diurnal cycles are relatively similar. In April and May BL heights are greater than the other months. The diurnal cycles in April and May are also less consistent.

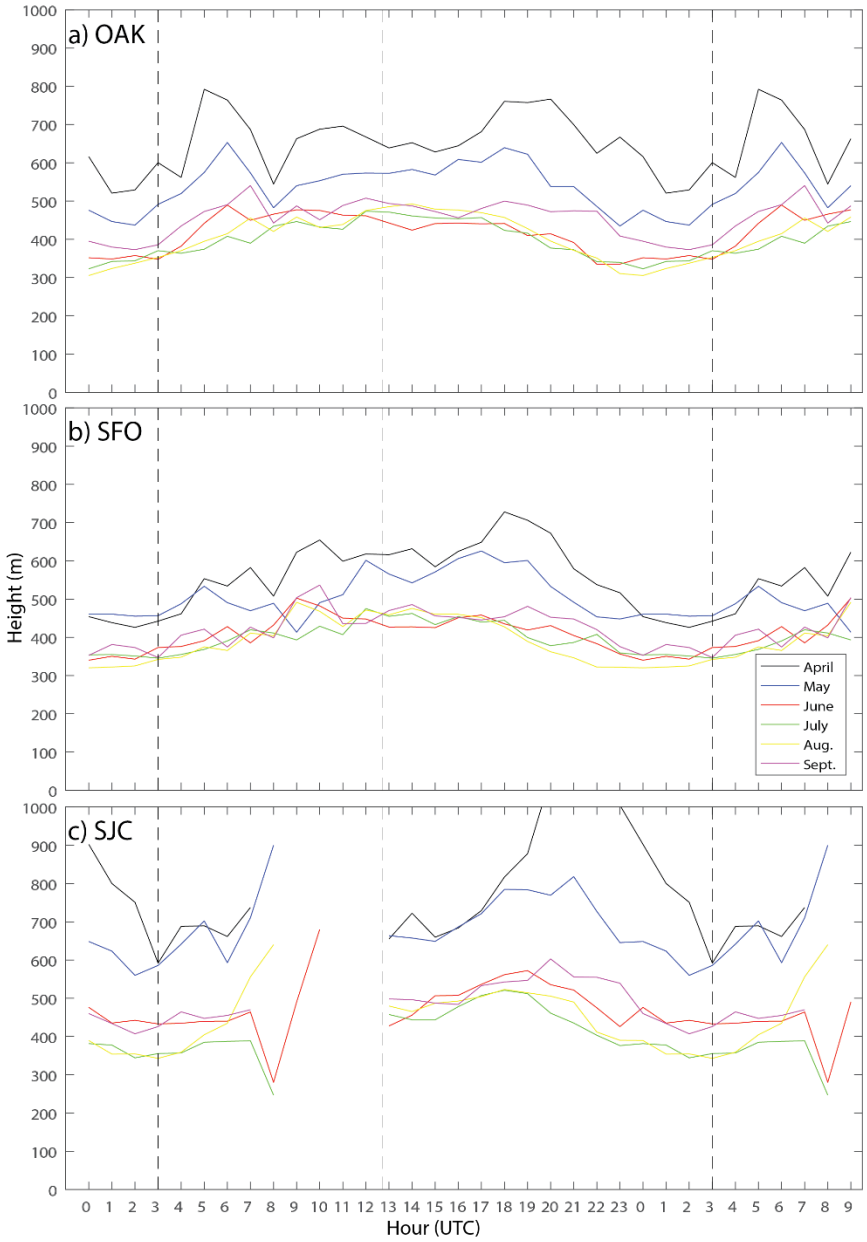

Fig. 3.5: The diurnal cycle of the average boundary layer height for all months during the warm season (April-September) at (a) OAK, (b) SFO, and (c) SJC. The vertical dashed bars indicate the sunrise and sunset on 15 June.

ii) SFO

At SFO there are also many soundings throughout the day, however, there are fewer soundings than at OAK. SFO is located at sea level 17 km to the southwest of OAK, across the San Francisco Bay. The interquartile range is similar to OAK with the smallest range around dusk (Fig. 3.4b). There are two peaks in mean BL heights, one right before dawn and the other at 1700 UTC. The main peak is the earlier one but BL heights slightly increase before 1700 UTC to create another peak. Following 1700 UTC, BL heights decrease rapidly to reach their lowest at dusk. At SFO the mean BL height is 413 m, the median is 368 m, and the standard deviation is 263 m.

The monthly diurnal cycle of BL heights at SFO are similar to those seen at OAK (Fig. 3.5b). The warmest months (June-September) are all very similar but there is a defined break between those months and April and May. However, the April and May BL heights show a clearer diurnal cycle that was not as evident at OAK. The mean diurnal BL heights from June through September range between 332 m and 527 m.

iii) SJC

SJC is located 46 km to the southwest of OAK, 47.9 km to the southwest of SFO, and 7.3 km inland from the southern point of the San Francisco Bay. There are zero soundings at SJC for 1100 UTC and 1200 UTC for all years during the study (Fig. 3.4c). As a result of very few soundings from 0800 UTC to 1200 UTC little can be said about BL heights at SJC during the early morning hours. Throughout the rest of the day there are a comparable number of soundings to those at SFO. BL heights are greatest at 1900 UTC, 2 hours after SFO and OAK experience their secondary peak in BL heights. At SJC, BL heights also are lowest around dusk. BL heights

are greater at SJC then at both SFO and OAK with a mean BL height for all soundings in June of 479 m, a median of 396 m, and a standard deviation of 284 m. The interquartile range is larger at SJC then at SFO and OAK.

The monthly diurnal cycle of BL heights also shows a clear break in BL heights between April and May and the warmest months (Fig. 3.5c). BL heights from June through September are greater than those at SFO and OAK. Not considering mean BL heights from 0800-1200 UTC because of the few observations, the mean BL heights during the day in the warmest months range from 384 m at 0300 UTC to 606 m at 1900 UTC.

b. Diurnal Cycle of Temperature and Wind

The diurnal cycle of temperature in June at SJC is noticeably different than that at OAK and SFO (Fig. 3.6). Temperatures are cooler at SFO and OAK throughout the day. At 1300 UTC temperatures within the BL are between 12-13°C at SFO and OAK while at the same time at SJC they range from 14-15°C. At SFO and OAK temperatures gradually increase throughout the day reaching their maximum of ~17°C at 2100 UTC. Temperatures at SJC increase more rapidly and reach their maximum of ~22°C at 2100 UTC. This indicates that soundings from SJC are more representative of a continental environment while SFO and OAK are more representative of a marine environment. The average temperature inversions at SFO, OAK, and SJC extend up to about 1100, 1300, and 1500 m, respectively. Above the temperature inversions there is little variability in the diurnal cycle.

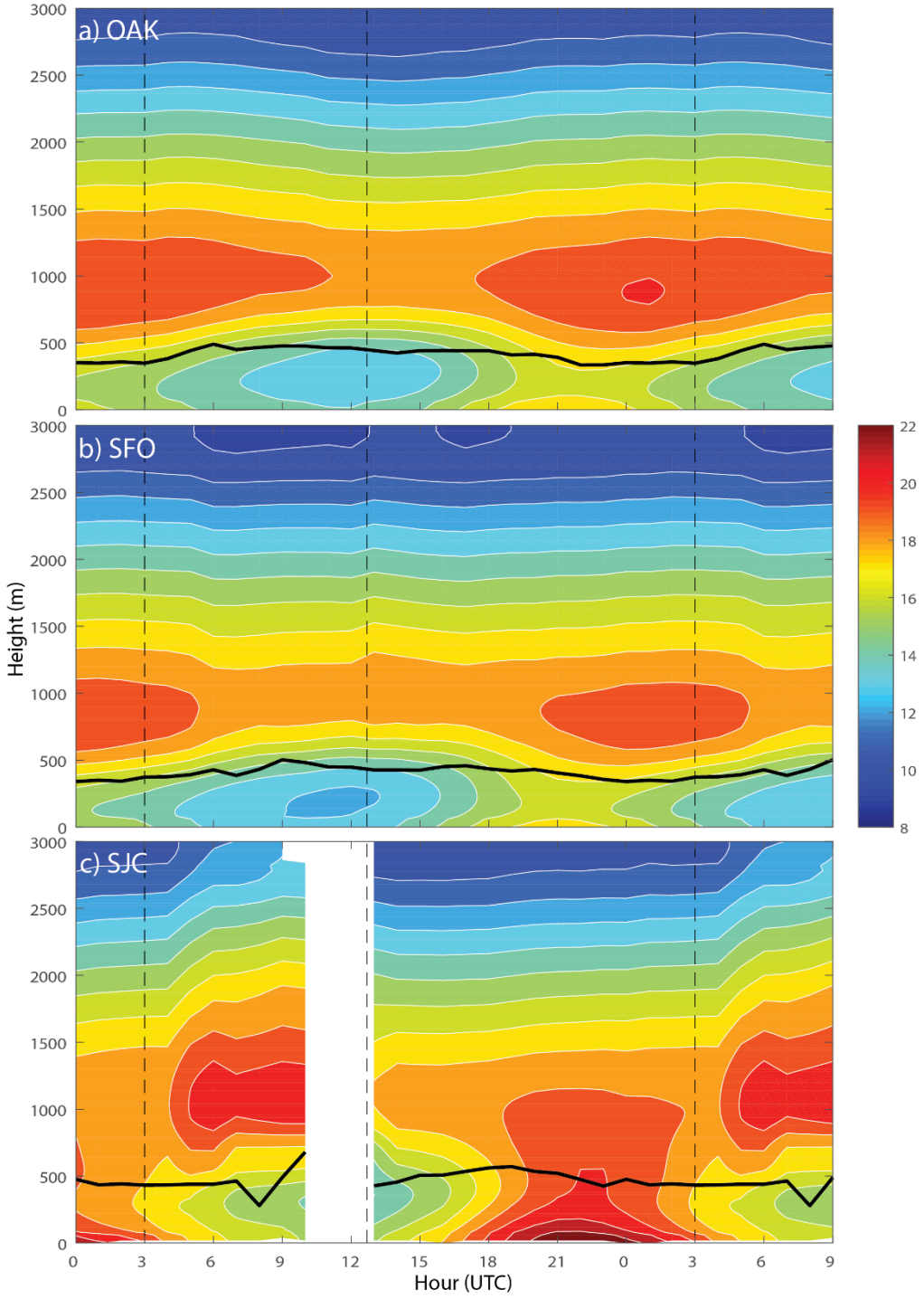

Fig. 3.6: Time-height cross sections of the temperatures at (a) OAK, (b) SFO, and (c) SJC in June from 2001-2016. The solid black line is the mean BL height for each airport in June. The vertical dashed bars indicate the sunrise and sunset on 15 June.

The diurnal cycles of the u-wind and v-wind components indicate the relationship between the BL and the wind (Fig. 3.7 and Fig. 3.8). There is a distinct diurnal cycle in both components at all three of the airports; however, there are differences between each airport. At 1200 UTC at OAK and SJC there is a negligible u-wind while there is a 2 m s^{-1} u-wind at SFO. Zonal winds within the BL reach a maximum at all three airports at 0000 UTC. SJC's u-wind component is far less than the other two airports, reaching only ~2 m s^{-1}. SFO reaches a maximum of 8 m s^{-1} while OAK reaches a maximum of 4 m s^{-1}. The stronger sea breeze at SFO is attributed to its closer proximity to the ocean. On average, a bay breeze does not appear to occur or have an effect on the sea breeze at SFO and OAK. The weak sea breeze at SJC can be attributed to the topography in between SJC and the Pacific Ocean. At all three airports the surface meridional wind is between 1 and 1.5 m s^{-1} at 1200 UTC. The BL at each airport is also capped by northerly flow. This flow is most pronounced at SFO and OAK with v-wind components of -3 to -4 m s^{-1}. By 0000 UTC all airports have a negative v-wind component but at SFO and OAK this component is weak (~-1 m s^{-1}). At SJC, northerly flow dominates at this time with a v-wind component of -4 m s^{-1}. Above the BL, at 0000 UTC, SJC also experiences southerly flow >1.5 m s^{-1}, indicating a broader circulation pattern affecting this region. This circulation appears to be a bay and valley breeze as a result of the land being able to heat up to ~22°C during the day.

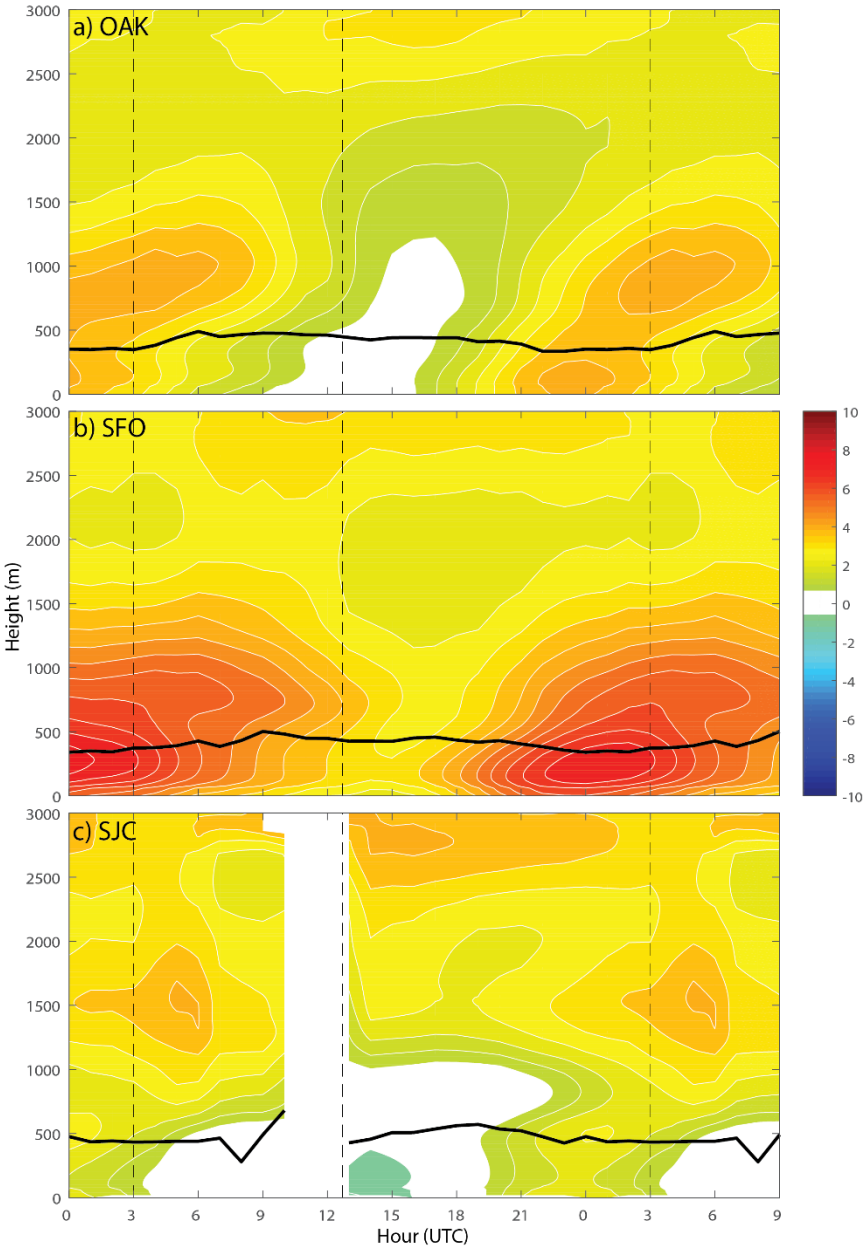

Fig. 3.7: Time-height cross sections of the u-winds at (a) OAK, (b) SFO, and (c) SJC in June from 2001-2016. The solid black line is the mean BL height for each airport in June. The vertical dashed bars indicate the sunrise and sunset on 15 June.

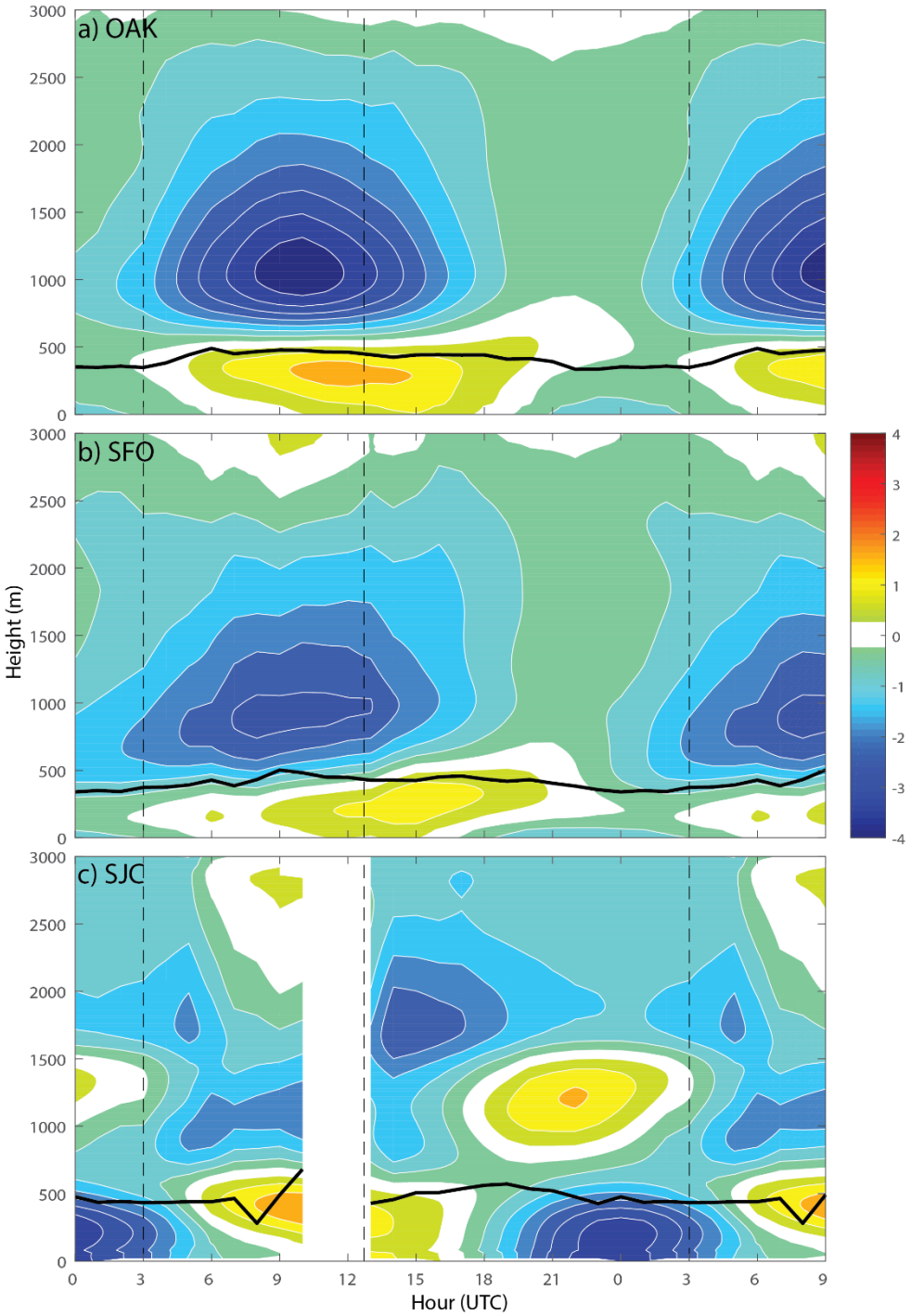

Fig. 3.8: Time-height cross sections of the v-winds at (a) OAK, (b) SFO, and (c) SJC in June from 2001-2016. The solid black line is the mean BL height for each airport in June. The vertical dashed bars indicate the sunrise and sunset on 15 June.

To better illustrate the differences in the diurnal cycles at each airport the diurnal cycles of each variable at SFO and SJC were subtracted from the corresponding variable at OAK (Fig. 3.9). The greater similarity between OAK and SFO compared to OAK and SJC can be seen. Temperatures between OAK and SFO only vary at most by 1° C where at SJC temperatures are warmer by more than 5° C. The u-wind at SFO is stronger than OAK by 4 m s^{-1} but in the mid-levels there are minor differences. At SJC the u-wind is weaker than OAK by 3 m s^{-1}. The v-wind diurnal cycle at SFO is more similar to OAK than SJC. The v-wind component at SJC is stronger than OAK by as much as 3 m s^{-1}.

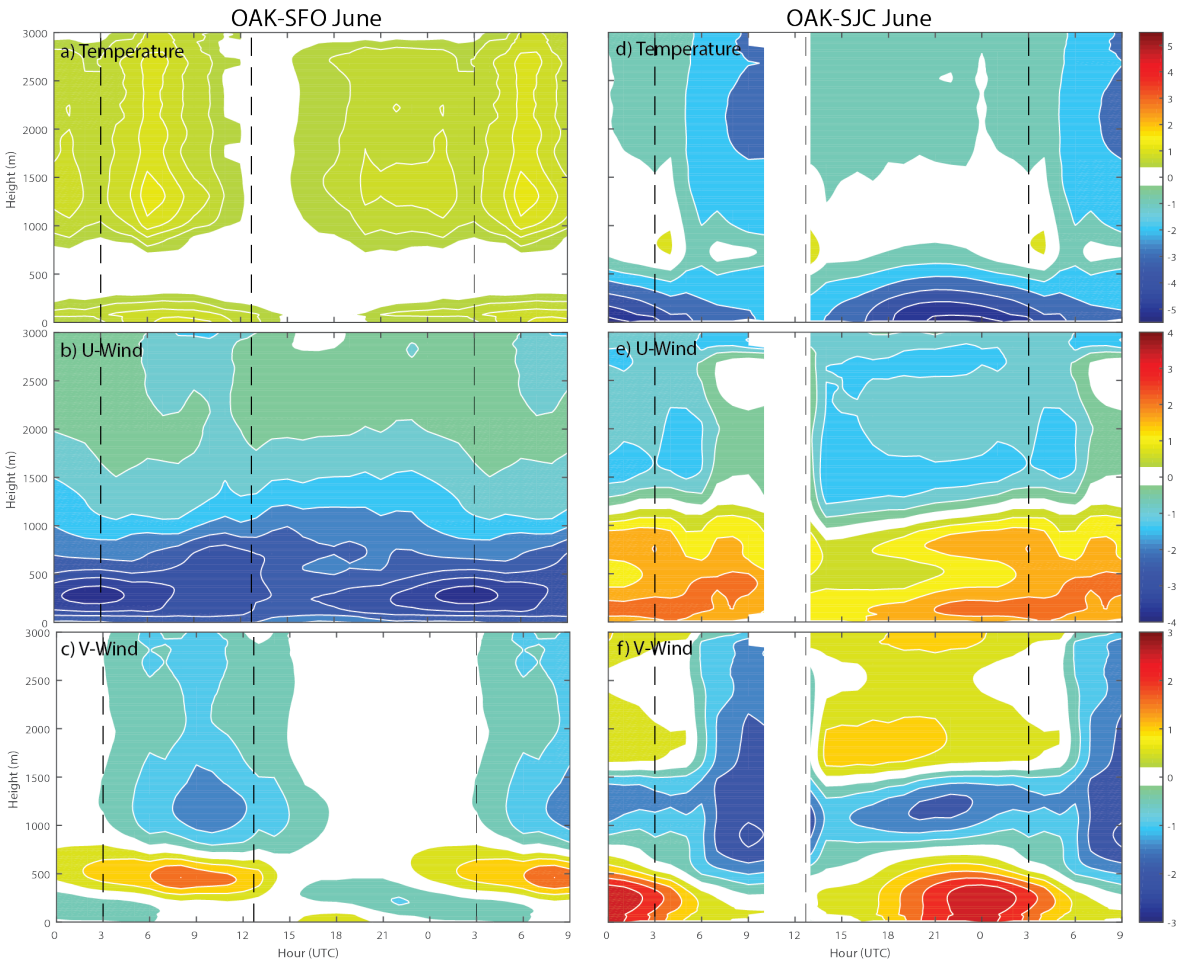

Fig. 3.9: (a-c) Time-height cross sections of the difference in the (a) temperatures, (b) u-winds, and (c) v-winds at OAK from those at SFO in June. (d-f) Time-height cross sections of the difference in the (d) temperatures, (e) u-winds, and (f) v-winds at OAK from those at SJC in June. The vertical dashed bars indicate the sunrise and sunset on 15 June.

3.3) Representativeness of AMDAR

The representativeness of the AMDAR data from each airport needs to be understood prior to using these measurements to analyze wind reversals. The twice daily NWS radiosonde launches at OAK will be considered the measurement benchmark for the AMDAR data. If the AMDAR data at OAK is highly correlated to the NWS soundings at OAK, and the AMDAR observations at the other airports (SJC and SFO) are highly correlated to the OAK AMDAR observations, then all airports can be grouped together to increase the number of observations included in the analysis.

Correlation profiles between OAK AMDAR observations and OAK NWS radiosondes, of the temperature, u-wind, and v-wind components were created for 0000 UTC and 1200 UTC during the warm season (Fig. 3.10). Since AMDAR observations do not typically fall perfectly on the hour, any observation between 1130 UTC to 1230 UTC was compared to the 1200 UTC radiosonde observations and those between 2330 UTC to 0030 UTC were compared against the 0000 UTC radiosonde observations. If more than one AMDAR profile occurred within the hour, the mean profile of each variable was used to have a more representative sounding of that hour.

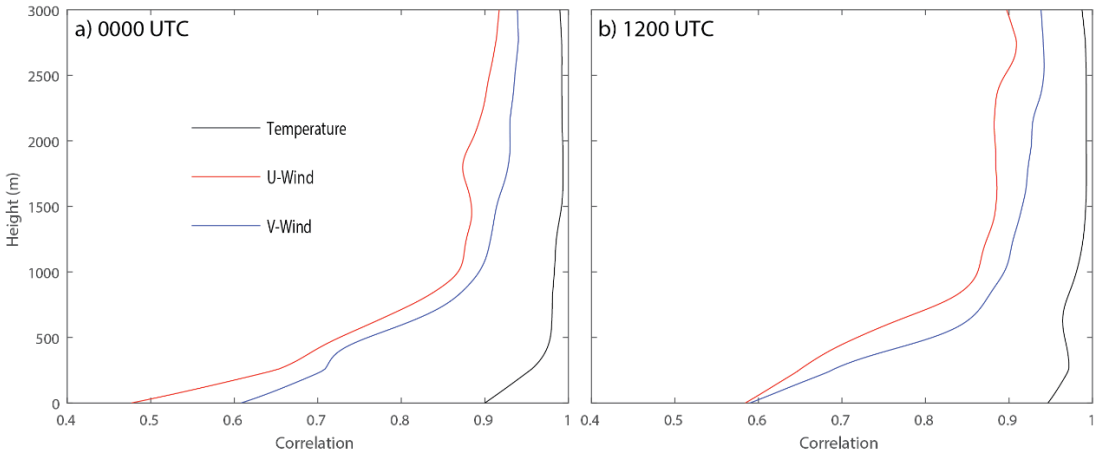

Fig. 3.10: Correlation profiles of temperature, u-wind, and v-wind during the warm season between AMDAR observations from OAK and NWS soundings from OAK at (a) 0000 UTC and (b) 1200 UTC.

Figure 3.10 indicates that at higher altitudes there is a high correlation between AMDAR and NWS radiosonde observations at OAK for temperature, u-wind, and v-wind components at 0000 UTC and 1200 UTC. Temperature is highly correlated at both times, with correlations >0.9 for the entire profile. The u-wind and v-wind components are less correlated than temperature; however, they are still highly correlated (>0.8) above the approximate height of the BL at both times. Since there is such a high correlation between OAK AMDAR observations and the NWS radiosonde observations, this provides confidence that there is little difference in the AMDAR data, especially above the BL. Furthermore, the horizontal displacement of the aircraft as it takes off or lands has negligible impact on the correlations when compared to the more vertical radiosonde observations. The correlations of the other airports, SFO and SJC, to the AMDAR observations at OAK were then analyzed to determine whether the observations can be combined.

The correlation profiles of temperature, u-wind, and v-wind components between OAK and SFO and between OAK and SJC were calculated by obtaining the mean profile of each variable for every hour during the warm season from 2001 through 2016. They were calculated over the entire warm season because the correlation profiles are not a function of the month. Correlations were calculated using the interpolated soundings with data every 20 meters from the surface to 3000 m (Fig. 3.11). The temperature profiles at SFO and SJC are highly correlated to OAK, with both having correlations >0.9 just above the surface through 3000 m. The profile of the v-wind component is more correlated between SFO and OAK with correlations >0.9 above 960 m. Between OAK and SJC the correlation of v-wind does not become >0.9 until 2380 m. The correlation profile of the u-wind component is also greater between SFO and OAK with

correlations >0.85 at 760 m. At SJC, the u-wind component is not very correlated (<0.8) until 1420 m above the surface and never becomes correlated >0.85.

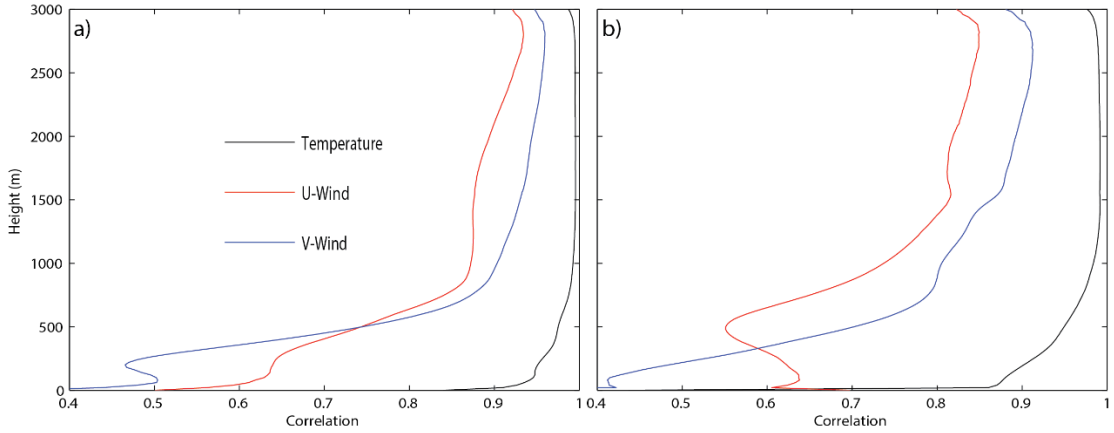

Fig. 3.11: Correlation profiles of temperature, u-wind, and v-wind at all hours during the warm season between (a) AMDAR observations at OAK and SFO and (b) AMDAR observations at OAK and SJC.

To illustrate the correlation between each airport and to examine the differences, density plots were created from the mean profiles of temperature, u-wind, and v-wind for every hour during the warm season. Density plots using observations at OAK and SFO within the BL (300 m) and above the BL (1000 m) were created (Fig. 3.12). Similar plots were created using data at OAK and SJC (Fig. 3.13). The density plots illustrate the generally higher correlations found above the BL as well as the higher correlations found between OAK and SFO than OAK and SJC. Temperatures at OAK and SFO are highly correlated with little difference within the BL and above the BL. Within the BL at SFO, the u-wind is generally higher than OAK. Above the BL the u-wind is highly correlated, but systematically different with the u-wind at SFO again higher than OAK. Poor correlation is found in the v-wind within the BL, but above the BL the observations are highly correlated with little difference.

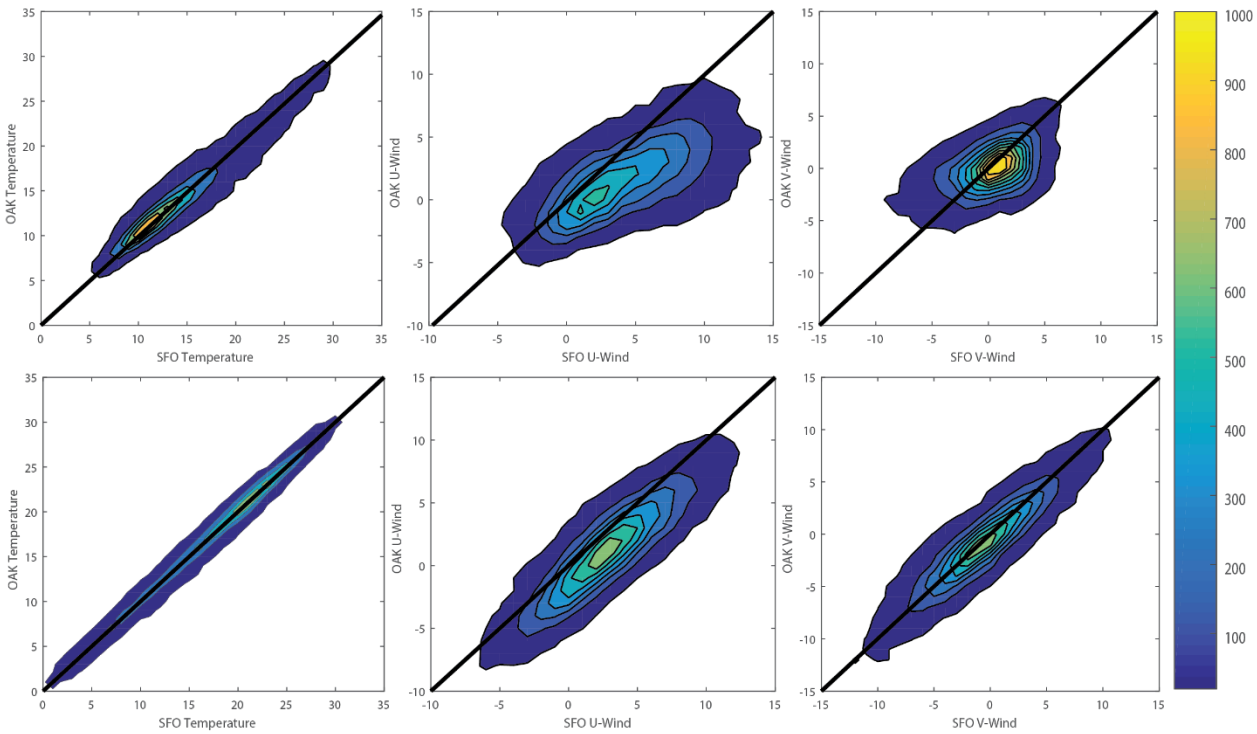

Fig. 3.12: Density plots of OAK's and SFO's temperatures, u-winds, and v-winds during the warm season from 2001-2016 (Top Row) within the BL at 300 m and (Bottom Row) above the BL at 1000 m. Temperatures are binned every 1° C and winds are binned every 1 m s^{-1}. The one to one reference line is shown in black.

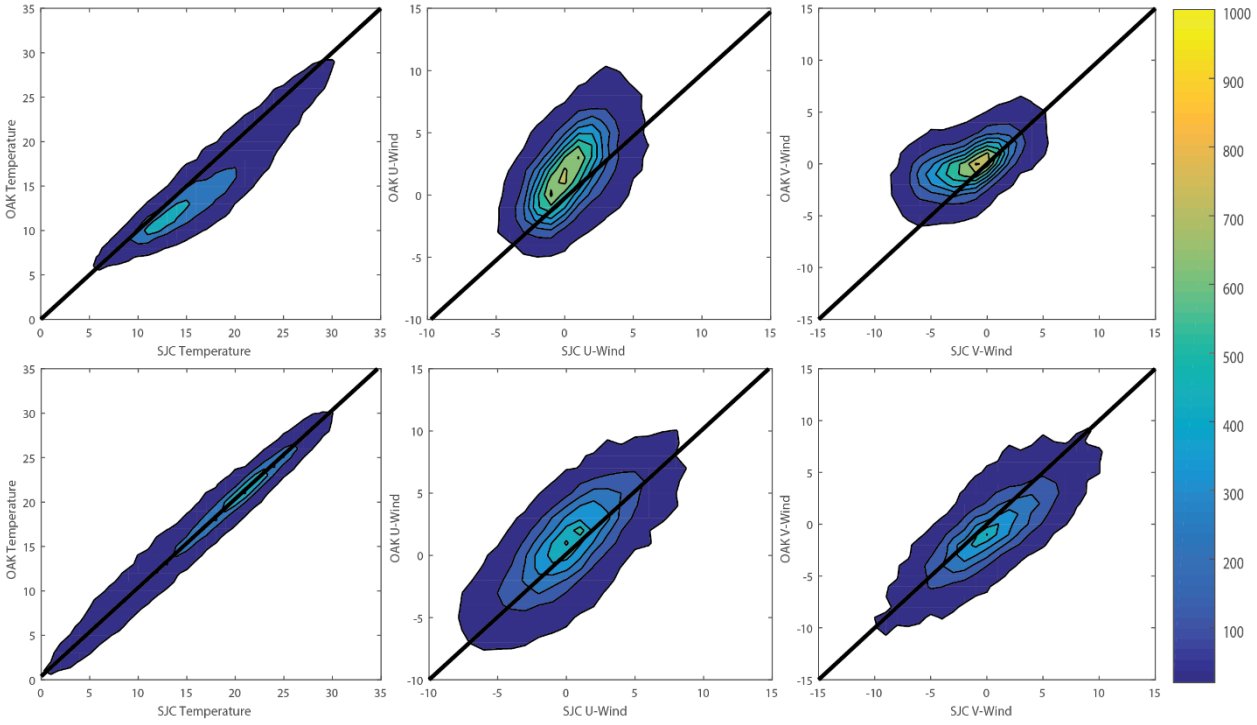

Fig. 3.13: Density plots of OAK's and SJC's temperatures, u-winds, and v-winds during the warm season from 2001-2016 (Top Row) within the BL at 300 m and (Bottom Row) above the BL at 1000 m. Temperatures are binned every 1° C and winds are binned every 1 m s^{-1}. The one to one reference line is shown in black.

The broader density plots between OAK and SJC indicate lower correlations of all three variables within the BL. The u-wind and the v-wind are generally lower at SJC than at OAK. Above the BL, there are better correlations between each variable. The temperature above the BL is highly correlated with little difference. The differences between the wind components is more diffuse. The u-wind at SJC is still slightly lower than at OAK in general. For the remainder of the analysis of wind reversals, since SFO is highly correlated to OAK at all heights above the BL (~500 m) their observations will be combined through linear averaging. However, as a result of the lower correlation in the wind components between SJC and OAK, the discrepancies in diurnal cycles, and the missing observations at peak wind reversal hours, SJC will not be a part of the remaining analysis of wind reversals.

Chapter Four

Wind Reversals

4.1) Anomalies

To calculate the anomalies before, during, and after reversals the temperature, u-wind, and v-wind component profiles from AMDAR observations taken from SFO and OAK 72 hours before to 72 hours after high and low threshold events were recorded relative to the time of wind reversal at the buoy. Mean hourly soundings for each month were calculated using SFO and OAK profiles since they were highly correlated, which greatly increased the sample size. Raw temperature, u-wind, and v-wind component profiles were subtracted from the mean hourly profile for the corresponding month to obtain the anomalies 72 hours before to 72 hours after each reversal. The mean anomaly profiles before and after high and low threshold events were then calculated (Fig. 4.1 and Fig. 4.2). The maximum average temperature anomaly for low threshold events is 3.5° C and occurs between 450 and 800 m 12 hours before a wind reversal. For high threshold events the maximum average temperature anomaly is 4° C 10 hours before a wind reversal ~500 m above the surface. For low and high threshold events there is a peak in the u-wind anomaly just above the BL of -2 m s^{-1} 24 h prior to the start of a reversal. Directly above the BL there is not a strong v-wind anomaly for either threshold events. However, 24 hours ahead of a reversal the v-wind anomaly does become > 0 m s^{-1} for low and high threshold events. Since there are defined anomalies 24 h before wind reversals occur a forecast metric based on just observed anomalies might be able to forecast them with a lead time of 1 day.

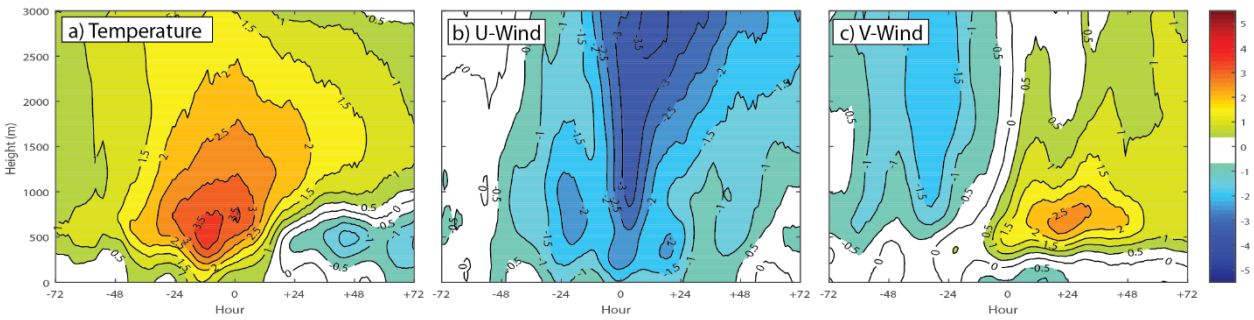

Fig. 4.1: Time-height cross sections of the mean anomalies of the (a) temperatures, (b) u-winds, and (c) v-winds before, during, and after the start of low threshold wind reversal events from AMDAR observations at OAK and SFO

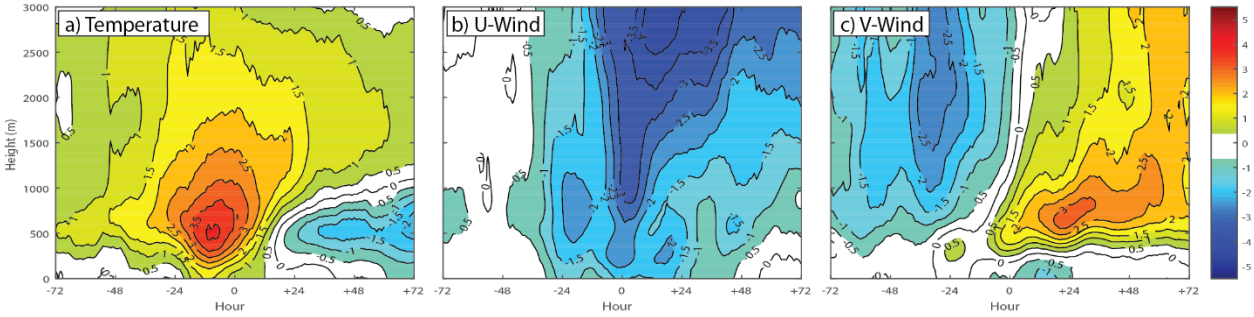

Fig. 4.2: As in Fig. 4.1 but for high threshold wind reversal events.

4.2) Significance

To test the significance of the mean anomaly profiles, two-sample t-tests were performed on the mean temperature, u-wind, and v-wind anomaly profiles 36, 24, 12, and 0 hours before high and low threshold wind reversals (Fig. 4.3 and Fig. 4.4). Any observation with a p-value < 0.01 was considered significant. The standard deviations of the mean anomalies were also calculated and plotted on Figure 4.3 and Figure 4.4. The standard deviations are large but the mean anomalies are significant for most of the variables up to 36 hours ahead of reversals.

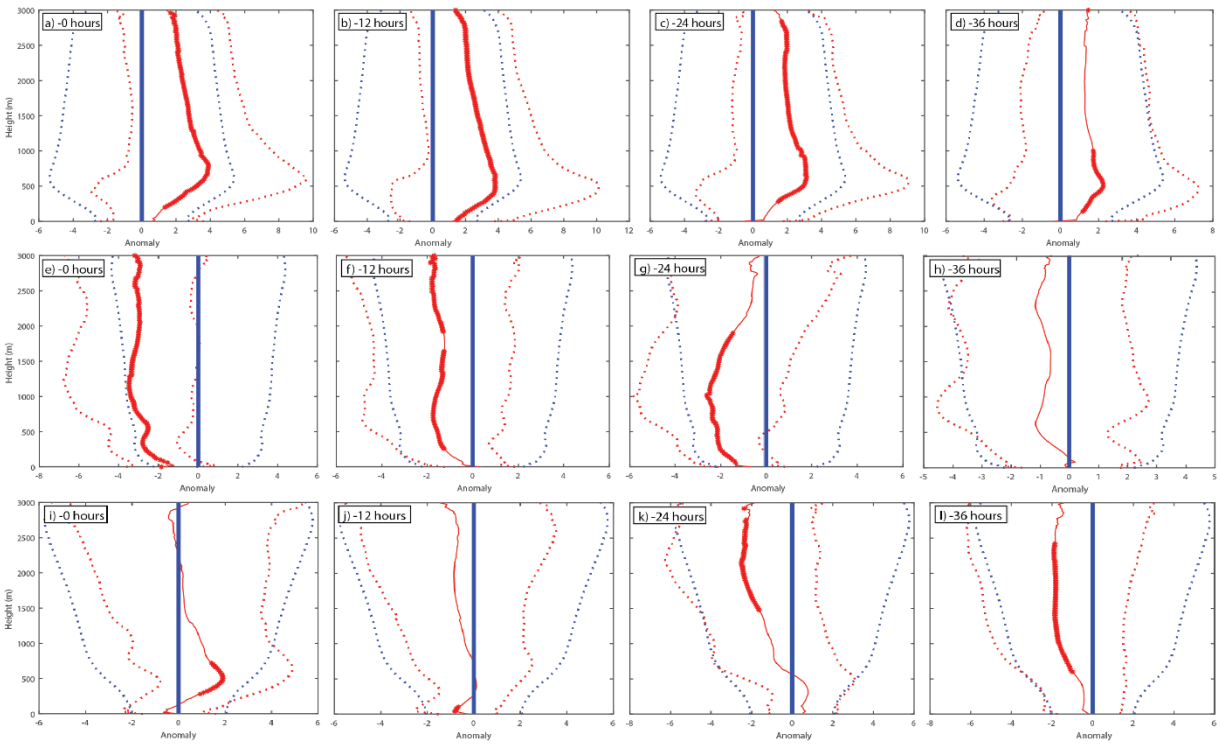

Fig. 4.3: The solid red line shows the mean anomaly profiles of the (a-d) temperature, (e-h) u-wind, and (i-l) v-wind for 0, 12, 24, and 36 hours before the start of low threshold wind reversal events. Where the solid red lines become thicker is where the mean anomalies of low threshold events are significant at the 0.01 level. The dashed red lines indicate the standard deviations of the mean anomalies. The solid blue line is the zero anomaly line and the dashed blue lines indicate the standard deviations of all observations during the warm season.

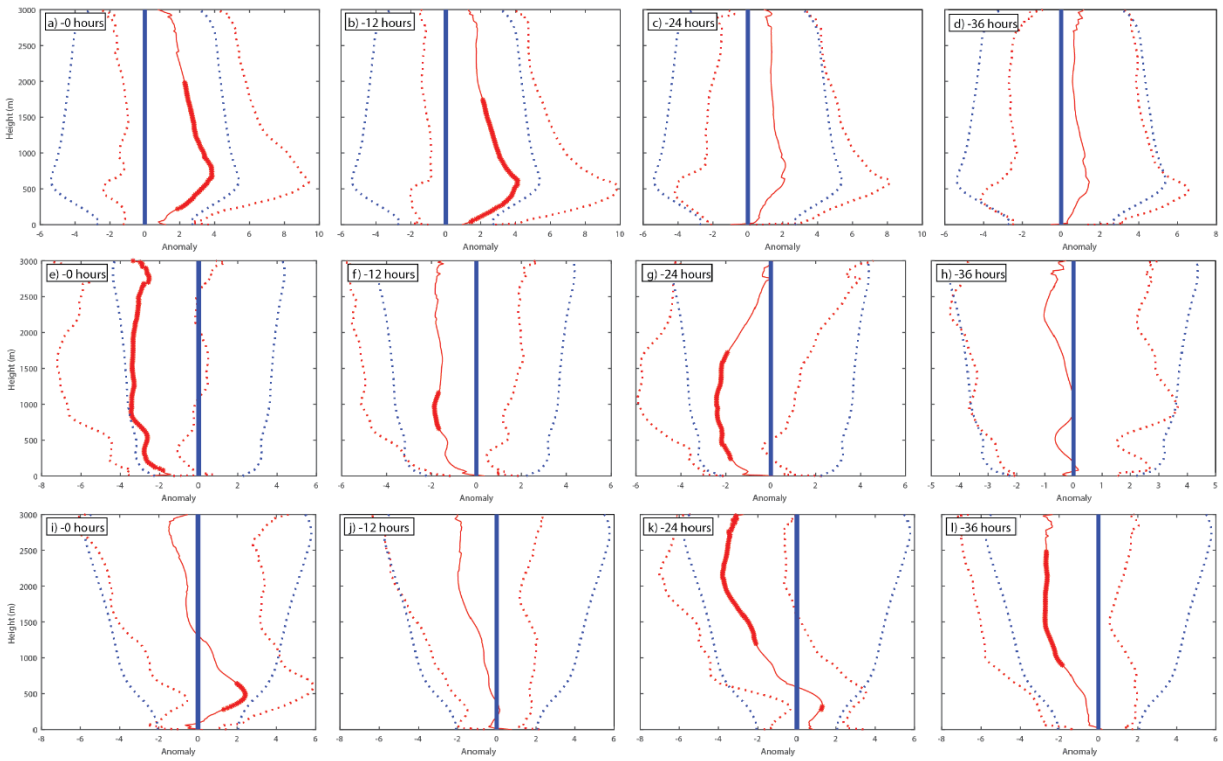

Fig. 4.4: The solid red line shows the mean anomaly profiles of the (a-d) temperature, (e-h) u-wind, and (i-l) v-wind for 0, 12, 24, and 36 hours before the start of high threshold wind reversal events. Where the solid red lines become thicker is where the mean anomalies of high threshold events are significant at the 0.01 level. The dashed red lines indicate the standard deviations of the mean anomalies. The solid blue line is the zero anomaly line and the dashed blue lines indicate the standard deviations of all observations during the warm season

4.3) Anomaly Forecast Metric

Since the mean anomalies of the temperature, u-wind, and v-wind profiles are significant above the BL for both low and high threshold wind reversal events a forecast metric was able to be created. Many different metrics were examined, but only the best performing forecast metric is presented. Using AMDAR observations, if between 400-1000 m there was a temperature anomaly >3.5° C, a zonal wind anomaly <-2.5 m s^{-1}, and a meridional wind anomaly >0 m s^{-1}, then a wind reversal was forecasted to occur, and the corresponding date was recorded. The same metric was used for low and high threshold events because the profiles of the atmosphere are

very similar between both strengths of events. Different metrics were tested for low and high threshold events, but both performed best under this metric.

The performance of the forecast metric was tested by first grouping forecasted dates into events since there are often consecutive hours of observations reaching the criteria of the forecast metric. Any forecasted dates that occurred within 12 hours of each other were considered part of the same wind reversal event and grouped together. The forecasted events were then compared to the recorded wind reversal events from 2001 through 2016. Reversals were considered correctly forecasted if within the forecasted event groupings a forecasted event date was more than 1 h ahead of a reversal and at least one forecasted event date was within the 36 h before a wind reversal event. Also, one forecasted event date from a grouping must be within the 36 h before a wind reversal event in order to ensure that the forecasted event grouping is associated with a specific reversal event so there are not unsubstantiated high lead times. The performance of the forecast metric for low and high threshold events is shown in Table 4.1. Low threshold events had a probability of detection (POD) of 59.8% and a false alarm ratio (FAR) of 79.2%. High threshold events had a POD of 66.0% and a FAR of 87.7%. Although the POD for both events is reasonable, the FAR is too high for the anomaly forecast metric to be of use.

Table 4.1: Contingency table showing the performance of the anomaly forecast metric.

	Low Threshold Events		High Threshold Events	
Forecasted Events	Occurred	Did not occur	Occurred	Did not occur
Forecasted	49	187	29	207
Not forecasted	33	x	15	x

Several issues may inhibit using the simple anomaly to create a reliable forecast metric. The anomalies have high variability and since the anomalies are confined to the bay area at 400-

1000 m, and these observations may not reflect the broader conditions that can be conducive for wind reversal formation. To examine the high variability in the anomalies, the quantiles of the mean anomalies were analyzed. The height of 760 m was chosen as this is just above the BL and this height is where all three variables have the greatest significance. The mean anomalies of the temperature, u-wind, and v-wind were then plotted along with the 10%, 25%, 75%, and 90% quantiles for 72 hours before to the start of low and high threshold reversals (Fig. 4.5 and Fig. 4.6). In Figure 4.5 and Figure 4.6, the spread of the anomalies is large, however, there is an observable change in the anomalies leading up to the start of the wind reversal. For both low and high threshold events the mean temperature anomalies steadily increase from <1°C 72 hours ahead of an event to ~4.0°C 6 hours ahead of an event. The mean anomalies of the u-wind component for both strengths of events also change in magnitude ahead of a reversal decreasing from -0.4 m s^{-1} 72 hours ahead to -2.3 m s^{-1} by the start of a reversal. However, the mean anomalies of the u-wind component do not uniformly decrease. For both low and high threshold events the mean anomalies of the v-wind components decrease from ~-1.0 m s^{-1} 72 hours ahead to ~-1.6 m s^{-1} 30 hours ahead of a reversal. They then steadily increase to ~1.6 m s^{-1} by the start of the reversal. Given the poor performance of the simple anomaly forecast metric but the clear changes in the anomalies, using a trend of the temperature, u-wind, and v-wind components to create a forecast metric was explored.

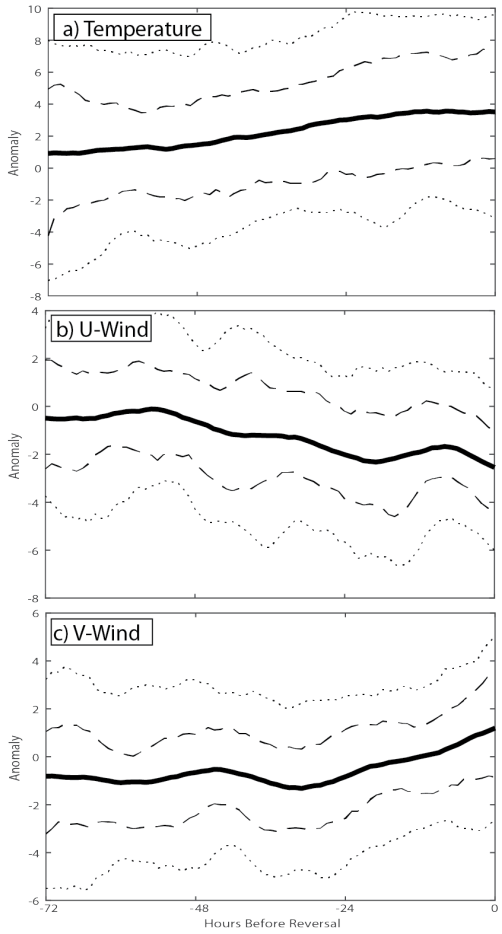

Fig. 4.5: The solid black line is the mean anomalies of the (a) temperature, (b) u-wind, and (c) v-wind leading up to the start of low threshold wind reversal events. The dashed lines are the 25% and 75% quantiles. The dotted lines are the 10% and 90% quantiles.

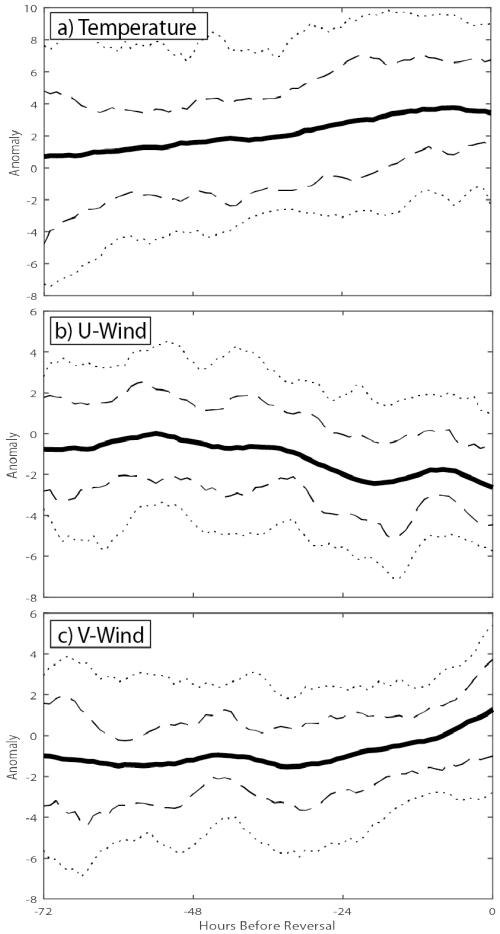

Fig. 4.6: As in Fig. 4.5 but for high threshold wind reversal events

4.4) Trend Forecast Metric

The trend was chosen to better represent pulses of the anomalous wind conditions from the recent state of the environment instead of the long-term climatology. The 3-, 6-, 9-, and 12-hourly mean trend of the anomalies for each variable at 760 m were calculated for both low and high threshold events (Fig. 4.7 and Fig. 4.8). Again, there is very little difference in the high and low threshold trend graphs. Figure 4.8a shows that the temperature trend is consistently positive

until 6 hours before the reversal. The most noticeable time is 40 hours ahead of the reversal when the temperature trend increases rapidly to >0.08°C h^{-1}. U-wind component trends fluctuate more but are mostly negative 54 hours ahead to 14 hours ahead of the reversal. The u-wind component trend reaches a minimum of ~-0.125 m s^{-1} h^{-1} 24 hours ahead of a reversal. The v-wind component trend increases over the 72 hours prior to a reversal but it also is not consistent. From 36 hours before to the start of the event however the v wind increases steadily from <-0.05 m s^{-1} h^{-1} to ~0.15 m s^{-1} h^{-1}. There is a visible diurnal cycle in both the u-wind and v-wind component trend graphs because the diurnal cycle is less exaggerated during a wind reversal.

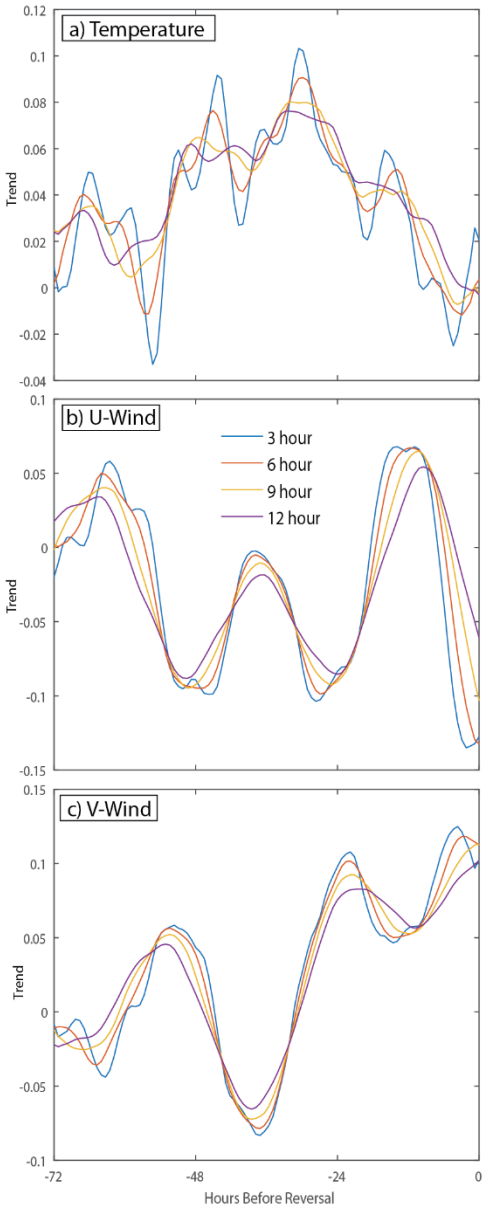

Fig. 4.7: The 3, 6, 9, and 12 hourly mean trend of the anomalies of the (a) temperature, (b) u-wind, and (c) v-wind leading up to the start of low threshold wind reversal events.

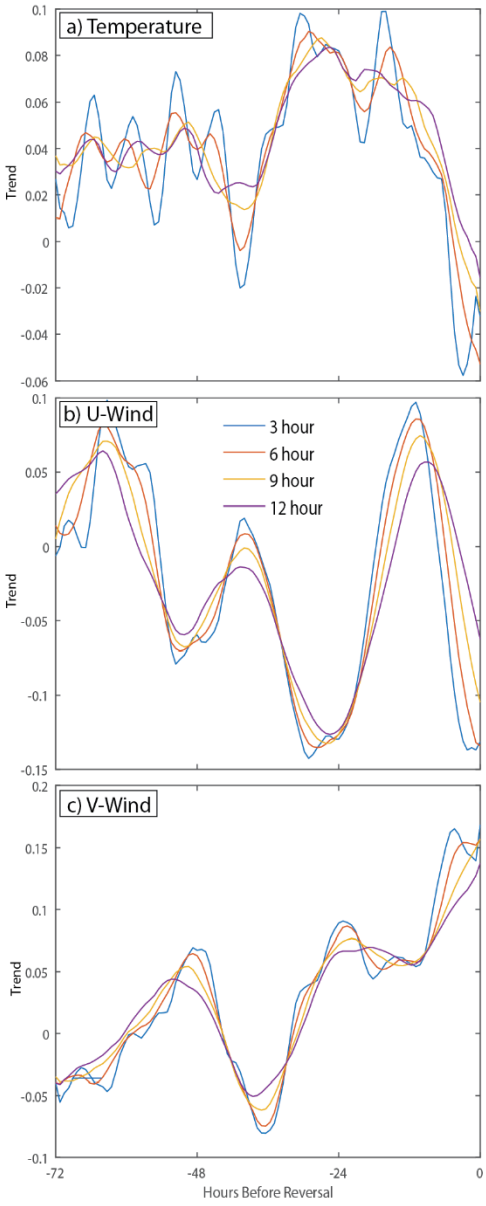

Fig. 4.8: As in Fig. 4.7 but for high threshold wind reversal events.

The trends of the temperature, u-wind, and v-wind component anomalies were then used to create a forecast metric. Various metrics were tested and the following was the best performing for both low and high threshold events. If over the prior hour the temperature anomaly increased more than 0.04°C, the u-wind component anomaly decreased by more than

0.04 m s^{-1}, and the v-wind component anomaly increased more than 0.02 m s^{-1} between 400 and 1000 m then a wind reversal was forecasted to occur. Once again, since there are often consecutive hours of observations reaching the criteria of the forecast metric, any forecasted dates that occurred within 12 hours of each other were considered one event and grouped together and reversals were considered correctly forecasted if within the forecasted event groupings a forecasted event date was more than 1 h ahead of a reversal and at least one forecasted event date was within the 36 h before a wind reversal event. Table 4.2 shows the performance of the metric for low and high threshold events. For low threshold events the POD is 30.5% and the FAR is 89.0%. For high threshold events the POD is 38.6% and the FAR is 92.5%.

Table 4.2: Contingency table showing the performance of the trend forecast metric.

	Low Threshold Events		High Threshold Events	
Forecasted Events	Occurred	Did not occur	Occurred	Did not occur
Forecasted	25	203	17	211
Not forecasted	57	x	27	x

Chapter Five

Summary and Conclusions

The climatological profile of the atmosphere and the diurnal cycle of the lower atmosphere of the San Francisco Bay region during the warm season was studied using NARR and AMDAR data. Wind reversals along the central California coast were also studied using AMDAR observations to quantify the precursors and to explore creating a simple forecast metric. AMDAR proved to be an excellent source of atmospheric observations. AMDAR observations from flights arriving or departing OAK, SFO, and SJC airports were used in this study due to their close proximity to the San Francisco Bay.

The first half of this paper presents the climatology of the San Francisco Bay and examines the representativeness of the AMDAR observations. To look at the climatology of the San Francisco Bay, upper air composite maps were created to show the synoptic conditions of the western United States and the eastern Pacific Ocean. June was chosen as the month of study because it is fairly representative of the rest of the warm season. The diurnal cycles of BL heights for each airport around the bay were then derived from the AMDAR observations. They showed that the highest BL heights occur in the morning while the lowest occur in the evening in the San Francisco Bay region. The diurnal cycle profiles of temperature and wind were then also created for each airport as well as the difference in the diurnal cycle profiles at SFO and SJC to OAK's profiles. There was less variation in OAK's and SFO's diurnal cycle profiles than OAK's and SJC's diurnal cycle profiles. Next, the representativeness of the AMDAR observations was analyzed. To look at the representativeness of the AMDAR observations the correlations of the observations from OAK to the NWS soundings at OAK were calculated. The AMDAR observations at OAK were found to be highly correlated to the NWS soundings at OAK.

Correlations between the observations at OAK and SFO as well as OAK and SJC were then calculated. SFO's and OAK's atmospheric profiles were found to be highly correlated and more similar to a marine environment. SJC was not as correlated to OAK and appeared to be more similar to a continental environment. Density plots were also created between OAK and SFO as well as OAK and SJC to further see the correlation and the difference between the different airports. More difference was found at SJC where the u-wind and v-wind within the BL is systematically lower than that at OAK. As a result of the differences in SJC to SFO and OAK, SJC observations were then not used in the analysis of wind reversals while SFO and OAK observations were then combined.

The second half of this paper focuses on the use of AMDAR observations to study wind reversals off the coast of San Francisco, California. Two classification schemes were used to study wind reversals. The first classification scheme, high threshold events, was based on Bond and Mass's (1996) classification of strong wind reversals. The second classification scheme, low threshold events, was created due to issues arising from Bond and Mass's (1996) classification scheme and was created by lowering the southerly wind threshold to 3 m s^{-1}. High and low threshold wind reversal event dates were then found using buoy data from off the coast of San Francisco, California. Next, temperature and wind anomaly profiles were created for before, during, and after high and low threshold wind reversal events. T-tests were performed to test the significance of these profiles. The profiles were found to be significant as early as 36 hours ahead of a reversal. They were mostly significant between 400 and 1000 m. Since the anomaly profiles were significant a forecast metric was then created using them. If a temperature anomaly >3.5° C, a zonal wind anomaly <-2.5 m s^{-1}, and a meridional wind anomaly >0 m s^{-1} were present between 400 and 1000 m then a wind reversal was forecasted to occur. This forecast

metric did well at detecting events, with a POD of 59.8% for low threshold events and a POD of 66.0% for high threshold events, but had too many false alarms. Since the anomaly forecast metric did not turn out to be a reliable metric the variability of the anomalies were analyzed to see if that is inhibiting its success. The mean anomalies and quantiles of the temperature and winds at 760 m leading up to high and low threshold wind reversal events were calculated. High variability amongst the anomalies was found, however, an observable trend in the anomalies was present. The trends of the anomalies were then quantified and used to create a second forecast metric. If over the prior hour between 400 and 1000 m the temperature anomaly increased more than 0.04°C, the u-wind component anomaly decreased more than 0.04 m s^{-1}, and the v-wind component anomaly increased more than 0.02 m s^{-1} then a wind reversal was forecasted to occur. This second forecast metric performed even worse than the anomaly forecast metric with a POD for low threshold events of 30.5% and a POD for high threshold events of 38.6% and higher FARs than the anomaly metric.

Although a viable forecast metric was not able to be created, more is now understood about the precursors and environment leading up to wind reversals. The AMDAR dataset has shown that it has a lot of potential for constructing climatologies and studying specific phenomenon such as wind reversals. With the increasing amount of observations and airlines adopting the AMDAR system it can be expected that more studies will focus on the use of this data.

REFERENCES

Angevine, W. M., L. Eddington, K. Durkee, C. Fairall, L. Bianco, and J. Brioude, 2012: Meteorological model evaluation for CalNex 2010. *Mon. Wea. Rev.,* **140,** 3885–3906.

Bond, N., C.F. Mass, and J. Overland, 1996: Coastally trapped wind reversals along the U.S. west coast during the warm season. Part I: Climatology and temporal evolution. *Mon. Wea. Rev.,* **124,** 430–445.

Bond, N., and C.F. Mass, 1996: Coastally trapped wind reversals along the U.S. west coast during the warm season. Part II: Synoptic evolution. *Mon. Wea. Rev.,* **124,** 446–461.

Dorman, C. E., 1985: Evidence of Kelvin waves in California's marine layer and related eddy generation. *Mon. Wea. Rev.,* **113**, 827–839.

Dorman, C. E., 1987: Possible role of gravity currents in northern California's coastal summer wind reversals. *J. Geophys. Res.,* **92**, 1497–1506.

Halliwell, G. R., Jr., and J.S. Allen, 1987: The large-scale coastal wind field along the west coast of North America, 1981-1982. *J. Geophys. Res.,* **92**, 1861–1884.

Neiburger, M., 1960: The relation of air-mass structure to the field of motion over the eastern North Pacific Ocean in summer. *Tellus,* **12**, 31–40.

Rahn, D. A., and C. J. Mitchell, 2016: Diurnal climatology of the boundary layer in Southern California using AMDAR temperature and wind profiles. *J. Appl. Meteor. Climatol.*, **55**, 1123–1137.

Rahn, D. A., and T. R. Parish, 2007: Diagnosis of the forcing and structure of the coastal jet near Cape Mendocino using in situ observations and numerical simulations. *J. Appl. Meteor. Climatol.*, **46**, 1455–1468.

Ralph, F. M., L. Armi, J. M. Bane, C. E. Dorman, W. D. Neff, P. J. Neiman, W. A. Nuss, and P. O. G. Persson, 1998: Observations and analysis of the 10–11 June 1994 coastally trapped disturbance. *Mon. Wea. Rev.,* **126,** 2435–2465.

Skamarock, W.C., R. Rotunno, and J. B. Klemp, 1999: Models of coastally trapped disturbances. *J. Atmos. Sci.,* **56,** 3349–3365.

Nuss, W. A., and Coauthors, 2000: Coastally trapped wind reversals: Progress toward understanding. Bull. Amer. Meteor. Soc., **81**, 719–743.

Wendell A. Nuss, 2007: Synoptic-Scale Structure and the Character of Coastally Trapped Wind Reversals. *Mon. Wea. Rev.*, **135**, 60–81.

Wyant, M.C., R. Wood, C. S. Bretherton, C. R. Mechoso, J. Bacmeister, M. A. Balmaseda, B. Barrett, F. Codron, P. Earnshaw, J. Fast, C. Hannay, J. W. Kaiser, H. Kitagawa, S. A. Klein, M. Kohler, J. Manganello, H.-L. Pan, F. Sun, S. Wang, and Y. Wang, 2010: The PreVOCA experiment: modeling the lower troposphere in the Southeast Pacific. *Atmos. Chem. Phys.,* **10**, 4757–4774.

APPENDIX

Low Threshold Wind Reversal Events 2001-2016

Year	Month	Day	Hour
2001	5	11	5
2001	5	19	16
2001	8	8	14
2001	9	7	16
2001	9	19	8
2002	4	1	12
2002	6	11	15
2002	7	2	7
2002	7	20	14
2002	7	27	15
2003	6	3	13
2003	8	31	8
2004	4	10	8
2004	6	16	15
2004	6	28	13
2004	8	8	11
2004	8	28	22
2005	5	25	12
2005	7	14	7
2005	7	17	8
2005	8	15	14
2005	9	8	6
2005	9	20	10
2006	5	4	2
2006	6	23	8
2006	7	26	10
2006	8	4	9
2006	8	13	9
2006	9	26	6
2007	7	6	9
2007	7	8	15
2007	8	23	17
2007	9	6	11
2008	6	13	4
2008	6	27	5
2008	7	8	6
2008	7	11	8
2008	9	8	9
2008	9	28	7
2009	6	30	5
2009	8	18	10
2009	9	9	8
2010	7	4	17
2010	7	10	9
2010	7	22	10
2010	8	1	12
2010	9	12	8
2010	9	29	12
2011	7	23	10
2011	7	27	9
2011	9	1	11
2011	9	10	3
2011	9	29	7
2012	7	23	9
2012	9	11	15
2012	9	23	6
2013	5	1	20
2013	6	3	7
2013	6	8	13
2013	7	21	10
2013	8	19	9
2014	6	10	6
2014	7	1	4
2014	7	8	14
2014	7	27	10
2014	8	4	7
2014	8	10	12
2014	8	23	9
2014	9	3	5
2014	9	20	8
2015	5	1	16
2015	6	5	13
2015	6	9	6
2015	6	26	4
2015	7	1	12
2015	8	7	3
2015	8	22	6
2016	6	12	12
2016	8	11	6
2016	8	17	14
2016	9	8	6
2016	9	13	5

High Threshold Wind Reversal Events 2001-2016

Year	Month	Day	Hour
2001	5	11	5
2001	9	7	16
2002	4	1	12
2002	6	11	15
2002	7	2	7
2002	7	20	14
2002	7	27	15
2003	6	3	13
2004	6	16	15
2004	6	28	13
2004	8	28	22
2005	7	14	7
2005	7	17	8
2005	9	20	10
2006	7	26	10
2006	8	4	9
2006	8	13	9
2006	9	26	6
2007	7	8	15
2007	9	6	11
2008	6	13	4
2008	6	27	5
2008	7	11	8
2009	6	30	5
2009	9	9	8
2010	7	4	17
2011	7	27	9
2011	9	10	3
2011	9	29	7
2012	7	23	9
2012	9	11	15
2013	6	3	7
2013	6	8	13
2013	8	19	9
2014	7	8	14
2014	8	10	12
2014	8	23	9
2015	6	5	13
2015	6	9	6
2015	6	26	4
2016	6	12	12
2016	8	11	6
2016	9	8	6
2016	9	13	5